



Solar radiation estimation in West Africa: impact of dust conditions during the 2021 dry season

Léo Clauzel¹, Sandrine Anquetin¹, Christophe Lavaysse¹, Gilles Bergametti², Christel Bouet^{2,3}, Guillaume Siour⁴, Rémy Lapere¹, Béatrice Marticorena⁴, and Jennie Thomas¹

¹IGE, Grenoble-INP, Université Grenoble Alpes, IRD, CNRS, 38000 Grenoble, France

²LISA, Univ Paris Est Créteil, Université Paris Cité, CNRS, 75013 Paris, France

³Institut d'Ecologie et des Sciences de l'Environnement de Paris, UMR IRD 242, Univ Paris Est Créteil, Sorbonne Université, Université Paris Cité, INRAE, CNRS, 93143 Bondy, France

⁴LISA, Univ Paris Est Créteil, Université Paris Cité, CNRS, 94010 Créteil, France

Correspondence: Léo Clauzel (leo.clauzel@univ-grenoble-alpes.fr) and Sandrine Anquetin (sandrine.anquetin@univ-grenoble-alpes.fr)

Received: 29 May 2024 – Discussion started: 10 June 2024

Revised: 13 November 2024 – Accepted: 14 November 2024 – Published: 27 January 2025

Abstract. The anticipated increase in solar energy production in West Africa requires high-quality solar irradiance estimates, which are affected by meteorological conditions and in particular the presence of desert dust aerosols. This study examines the impact of incorporating desert dust into solar irradiance and surface temperature estimations. The research focuses on a case study of a dust event in March 2021, which is characteristic of the dry season in West Africa. Significant desert aerosol emissions at the Bodélé Depression are associated with a Harmattan flow that transports the plume westwards. Simulations of this dust event were conducted using the meteorological Weather Research and Forecasting (WRF) Model alone, as well as coupling it with the CHIMERE chemistry transport model, using three different datasets for the dust aerosol initial and boundary conditions (CAM5, GOCART, and MERRA-2). Results show that considering desert dust reduces estimation errors in global horizontal irradiance (GHI) by about 75 %. The dust plume caused an average of 18 % reduction in surface solar irradiance during the event. Additionally, the simulations indicated a positive bias in aerosol optical depth (AOD) and PM₁₀ surface concentrations. The choice of dataset for initial and boundary conditions minimally influenced GHI, surface temperature, and AOD estimates, whereas PM₁₀ concentrations and aerosol size distribution were significantly affected. This study underscores the importance of incorporating dust aerosols into solar forecasting for better accuracy.

1 Introduction

The West African region is facing significant development challenges due to global changes. One of these challenges is related to access to electricity, particularly through the use of renewable energy. West African countries have committed to reducing their greenhouse gas emissions as part of the Paris Agreement (UNFCCC, 2015). Furthermore, assessments of solar resources in West Africa demonstrate the region's substantial potential, as shown by Diabaté et al. (2004), Plain et al. (2018), and Yushchenko et al. (2018). The International

Energy Agency (IEA) projects that the installed capacity for photovoltaic (PV) power generation will increase by almost 20 times from 2020 to 2030 under its Sustainable Africa Scenario (IEA, 2022). PV energy is expected to experience significant growth due to its competitiveness and low-carbon nature. However, solar production is highly dependent on weather conditions (Dajuma et al., 2016).

The growth of solar energy in West Africa calls for the development of tailored tools to facilitate its integration into power grids and ensure optimal operational maintenance. Accurate production forecasts are required by solar power

plant operators and have to span various timescales that range from a few hours to several days. This is essential for maximising production, reducing penalties linked to predicted deliverable energy, and optimising plant maintenance to minimise production losses. High-quality forecasts are also crucial for electricity grid operators to maintain supply–demand equilibrium and ensure system stability. Therefore, the variability in the energy production significantly affects them. The key meteorological variables that influence photovoltaic production are the global horizontal irradiance (GHI) and the air temperature. These factors, which directly impact electricity production and cell efficiency, often reach high levels in this region, as demonstrated by Dajuma et al. (2016) and Ziane et al. (2021). Their findings indicate that solar irradiance is the primary factor influencing PV production as the generated current by the photoelectric effect is proportional to the irradiance. Furthermore, they demonstrate that the second factor of air temperature affects the efficiency of solar cells as both parameters are inversely correlated.

Clauzel et al. (2024) identified desert dust aerosol as a significant source of GHI forecast errors for the only two solar power plants in the Sahel region of Sococim (Senegal) and Zagtouli (Burkina Faso), particularly during the dry season. Dust aerosols are a key element in the West African climate and strongly influence solar farm production through their direct effect (aerosol–radiation interaction (ARI); Briant et al., 2017) and indirect effects (aerosol–cloud interaction (ACI); Tuccella et al., 2019) on radiation, as well as also through their deposition on solar panels (fouling effect; Diop et al., 2020; Aidara et al., 2023). As mentioned by Kok et al. (2021), the West African desert aerosol load is the highest in the world and occurs mainly during the dry season. In fact, North Africa, including the Sahara, is the world's largest contributor to desert dust emissions (Prospero et al., 2002), and 60 % of this dust is transported to the West African region (D'Almeida, 1986; Kok et al., 2021). Most dust emissions are associated with synoptic-scale atmospheric dynamics such as the Harmattan flow during the dry season (Klose et al., 2010). Engelstaedter and Washington (2007) pointed out the importance of small-scale wind events associated with the large-scale flow, especially in the Bodélé Depression, which is a hotspot for dust emissions (Engelstaedter et al., 2006). Through analysing satellite observations, Schepanski et al. (2009) show that 65 % of the activation of the dust source area occurred in the early morning, demonstrating the important role of the breakdown of the nocturnal low-level jet. Washington and Todd (2005) confirmed the importance of the Bodélé low-level jets during the dry season for initiating dust emissions that can be transported to the West African coast within a few days. Dust aerosol emissions are also highly linked to mesoscale convective systems (MCSs; Marsham et al., 2008; Bergametti et al., 2017) and to strong near-surface winds in the intertropical discontinuity zone during the rainy season (Bou Karam et al., 2009).

Some studies intend to model dust events in West Africa, such as the one by Ochiegbu (2021), who implemented a back-trajectory model to understand the dust event reaching Nigeria. This work revealed that most of the aerosols coming to Nigeria between 2011 and 2014 originated from the Bodélé Depression. Menut (2023) focused on dust forecasting during the Clouds–Atmospheric Dynamics–Dust Interactions in West Africa (CADDIWA) campaign during the summer of 2021 (Flamant et al., 2024), using the CHIMERE regional chemistry transport model (Menut et al., 2021). The model was coupled online with the Weather Research and Forecasting (WRF) meteorological model (Briant et al., 2017; Tuccella et al., 2019) to perform dust aerosol concentration forecasts. The results of this work provide confidence in the model coupling in the region as the dust forecast quality does not decrease with time (up to a few days). In addition, only a limited number of studies has been conducted on the prediction of GHI in the West African region. Sawadogo et al. (2024) conducted an evaluation of WRF–Solar GHI forecast (Jimenez et al., 2016) in Ghana for the year 2021. In their work, a version of the model coupled offline with the Copernicus Atmosphere Monitoring Service (CAMS) aerosol optical depth (AOD) forecasts was considered to integrate information on aerosol load. They showed that WRF–Solar outperforms when predicting GHI under clear-sky conditions, while its performance under high aerosol levels remains poor; this was mainly attributed to uncertainties in the input AOD during data assimilation within the model. Close to the region of interest, for the northern Morocco area, El Alani et al. (2020) compared the performance of global models (Global Forecast System, Integrated Forecast System, and McClean) and demonstrated their proficiency in capturing GHI hourly temporal variability.

To our knowledge, no studies have been conducted to assess online coupled simulations between a meteorological model and an aerosol life cycle model representing the emissions, transport, and deposition in West Africa to estimate solar irradiance. This is despite the significant presence of desert dust characterised by high concentrations in the region. Additionally, hardly any attention has been given to the significance of initial and boundary conditions for conducting the aerosol model on the performance of analysis simulations, and to our knowledge, investigating these aspects would represent a novel contribution to research in the West African region.

Within this general context, the objectives of this study are two-fold: (i) to evaluate the ability to reproduce a dust event using a meteorological and dust life cycle model coupling configuration and (ii) to investigate whether the performance of the simulations can be enhanced by modifying the aerosol initial and boundary conditions employed and to estimate the uncertainty associated with this dataset selection with regard to the errors made by the model. Section 2 introduces the case study, the simulation configuration, the data, and the models selected for this work. In Sect. 3, the results are presented,

beginning with the variables of interest for solar production (GHI and surface air temperature), followed by the variables associated with the desert aerosols (AOD, concentration, size distribution, and emissions). Section 4 draws the main conclusions and gives some perspectives for this study.

2 Material and methods

2.1 Case study

The case study is a dust event that occurred in West Africa from 26 March 2021 at 00:00 UTC to 2 April 2021 at 00:00 UTC, i.e. during the dry season. High dust emissions occur at the Bodélé Depression (Chad), with the plume then being transported westward. The dust plume reached its maximum intensity in terms of AOD and dust concentration over West Africa and in particular over the Zagtouli solar farm (Burkina Faso; Fig. S1 in the Supplement) on 30 March 2024. The event was also chosen because it was not predicted in the solar forecast currently implemented for the Zagtouli solar farm, leading to solar forecast errors during the passage of the dust plume (Clauzel et al., 2024).

Figure 1 illustrates that this event is characterised by a strong Harmattan flow, with surface winds from the south/southwest sweeping across the Bodélé Depression (Chad), where the potential for desert dust emissions is very high (Prospero et al., 2002; Washington et al., 2006). Additionally, this event is characterised by a westward flow between Chad and the Atlantic coast, which facilitates the transportation of the dust plume. Figure 1a shows the Moderate Resolution Imaging Spectroradiometer (MODIS) satellite observations of the AOD, identifying the initial dust source area on the Bodélé Depression, as well as the westward movement of the plume. This event is characteristic of the West African dry season climatology, with a dominant Harmattan flow as described in Sect. 1. Figure S1 provides further insight into the dust plume transport during the case study.

2.2 Modelling tools

In order to reproduce a dust event during the dry season in West Africa, the WRF–CHIMERE coupled model is selected as it has previously demonstrated favourable performance in similar studies such as those conducted by Briant et al. (2017) and Menut (2023). The technical details of this coupled model are provided below.

2.2.1 WRF model

The meteorological Weather and Research and Forecasting (WRF) Model version 3.7.1 is taken for compatibility with the CHIMERE coupling procedure. It is used in its non-hydrostatic configuration (Skamarock et al., 2008), and it is forced at the boundaries of the domain every hour by the me-

teorological reanalysis data of ERA5 (ECMWF) provided on a regular $0.25^\circ \times 0.25^\circ$ grid.

The model is run with a 9 km horizontal resolution, a 45 s integration time step, and 50 vertical levels from the surface to 50 hPa. The updated rapid radiative transfer model for GCMs (RRTMG) radiation scheme (Iacono et al., 2008), which is mandatory for the aerosol optical property feedback, is employed for long- and shortwave radiations. Additionally, the Thompson aerosol-aware microphysics scheme (Thompson and Eidhammer, 2014) is applied. The Yonsei University planetary boundary layer's surface layer scheme (Hu et al., 2013) is also used, and the cumulus parameterisation is based on the Grell–Freitas scheme (Arakawa, 2004). The revised MM5 surface layer scheme (Jiménez et al., 2012) is employed, while the Noah-MP land surface model (Niu et al., 2011) is implemented for the land surface physics scheme.

2.2.2 CHIMERE model

The chemistry transport model CHIMERE version v2020r3 (Menut et al., 2021) is used in conjunction with the WRF model. Both models have a 9 km horizontal grid. The CHIMERE model has 30 pressure-dependent vertical levels from the surface up to 200 hPa, with a first layer thickness of 3 hPa. The model is configured for dust only, with no chemistry and only considering dust aerosols (details in Sect. 2.3). The threshold friction velocities for dust emissions are estimated using the Shao and Lu (2000) scheme and the 6 km spatial resolution GARLAP (Global Aeolian Roughness Lengths from ASCAT and PARASOL) dataset from Prigent et al. (2012). Mineral dust emission fluxes were calculated employing the Alfaro and Gomes (2001) scheme on 10 aerosol size bins ranging from 0.01 to 40 μm . The Fécan et al. (1999) parameterisation is employed to account for the inhibitory effect of soil moisture on dust emission. Dry deposition is treated as described in Zhang et al. (2001). Wet scavenging for aerosol is computed following the Willis and Tattelman (1989) scheme. The CHIMERE model includes the Fast-JX module, version 7.0b (Wild et al., 2000; Bian and Prather, 2002), for the calculation of radiative processes. It considers the radiative properties for each aerosol species and each aerosol size bin independently to compute the aerosol optical depths, the single-scattering albedo, and the aerosol asymmetry factor. More details on the dust aerosol radiative properties are given in Tables S1 and S2. Table 1 summarises the parameterisations employed in WRF and CHIMERE. Finally, we test three different initial and boundary condition datasets for the mineral dust load (see Sect. 2.2.3).

2.2.3 Dust aerosol initial and boundary condition datasets

In this study, the uncertainty in the solar estimate associated with the initial and boundary conditions of the dust aerosol

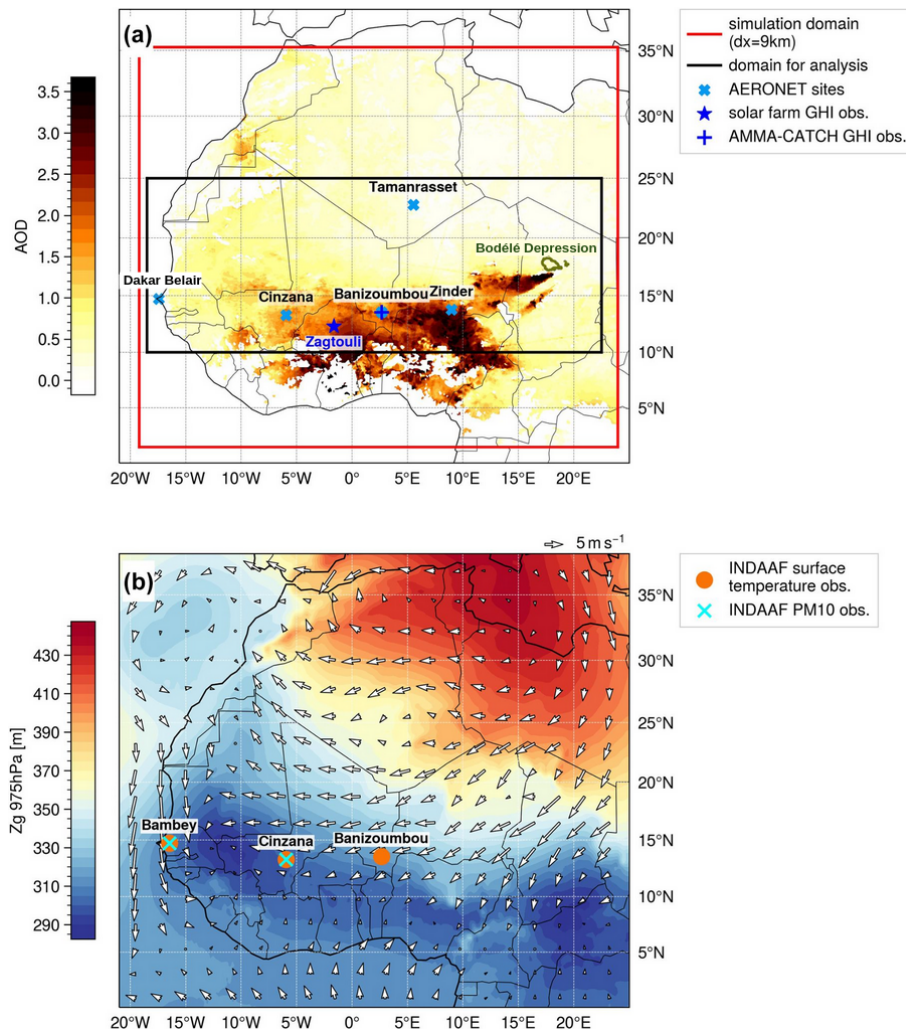


Figure 1. (a) Mean aerosol optical depth at 550 nm from MODIS satellite observations over the period from 28 March 2021 at 00:00 UTC to 2 April 2021 at 00:00 UTC. The global horizontal irradiance (GHI) observations and AERONET aerosol measurement network, introduced in Sect. 2.4, are presented, as well as the boundaries of the simulated domain (red rectangle) and the area of interest for analysis (black rectangle). (b) Mean synoptic conditions of the geopotential height (Z_g) at 975 hPa and the 10 m wind (white arrows; in m s^{-1}) over the period from 28 March 2021 at 00:00 UTC to 2 April 2021 at 00:00 UTC from ERA5 reanalysis. The surface temperature and aerosol concentration observations from the INDAAF network, introduced in Sect. 2.4, are presented.

load are evaluated. Three datasets were used, namely a climatology derived from the Global Ozone Chemistry Aerosol Radiation and Transport (GOCART; Ginoux et al., 2001), the Modern-Era Retrospective analysis for Research and Applications Version 2 (MERRA-2) reanalysis (Gelaro et al., 2017), and the CAMS reanalysis (Inness et al., 2019).

The GOCART climatology is provided with the distribution of the CHIMERE model. It is a monthly climatology on a coarse horizontal grid ($2^\circ \times 2.5^\circ$), which is corrected by applying a factor of 0.3 as in Vautard et al. (2005).

The MERRA-2 reanalysis combines the Goddard Earth Observing System (GEOS) and GOCART models, which are coupled online and implemented with a data assimilation system. It has a 3 h temporal resolution and is presented on a

$0.5^\circ \times 0.635^\circ$ horizontal grid. The observational data considered in the data assimilation process are AOD satellite observations from MODIS, the Advanced Very High Resolution Spectroradiometer (AVHRR), the Multi-angle Imaging SpectroRadiometer (MISR), and ground observations from the Aerosol RObotic NETWORK (AERONET).

The CAMS reanalysis was constructed using 4D-Var data assimilation in the ECMWF's Integrated Forecast System (IFS). It has a temporal resolution of 3 h and is computed on a regular 0.75° horizontal grid. The AOD data from the Visible Infrared Imaging Radiometer Suite (VIIRS), MODIS, and the Infrared Atmospheric Sounding Interferometer (IASI) satellite observations are used as observational information

Table 1. Parameterisations used in WRF and CHIMERE.

WRF	
Microphysics	Thompson aerosol-aware scheme (Thompson and Eidhammer, 2014)
Radiation	RRTMG scheme for LW and SW (Iacono et al., 2008)
Land surface	Noah-MP land surface scheme (Niu et al., 2011)
Planetary boundary layer	Yonsei University scheme (Hu et al., 2013)
Surface layer	Revised MM5 surface layer scheme (Jiménez et al., 2012)
Cumulus	Grell–Freitas scheme (Arakawa, 2004)
CHIMERE	
Threshold friction velocities	Shao and Lu (2000) scheme
Soil moisture	Fécan et al. (1999) scheme
Dust emission fluxes	Alfaro and Gomes (2001) scheme
Radiative processes	Fast-JX model, version 7.0b (Wild et al., 2000; Bian and Prather, 2002)
Aerosol size distribution bins (diameters in μm)	0.010–0.022 0.022–0.048 0.048–0.107 0.107–0.235 0.235–0.516 0.516–1.136 1.136–2.500 2.500–5.000 5.000–10.00 10.00–40.00

in the data assimilation process. Version 48R1 of CAMS is used in this study.

These three dust aerosol initial and boundary datasets differ in type (climatological or reanalysis); in the horizontal, vertical, and temporal resolutions; and in the resolution and range of their aerosol size distribution. While GOCART has the highest number of aerosol classes with seven bins, CAMS covers a wider size spectrum despite a lower size resolution with only three classes. MERRA-2 has an intermediate resolution with five classes but covers a smaller particle size spectrum than CAMS. The CHIMERE model pre-processes these dust aerosol size distributions by applying a transfer coefficient δ to compute the dust aerosol concentration on the 10 aerosol size bins defined for the simulations as follows:

$$c_j = \sum_i \delta_{i,j} \times c_i, \quad (1)$$

where c_i is the dust aerosol concentration of the i th size bin from the initial and boundary condition datasets considered, c_j is the dust aerosol concentration of the j th size bin in the CHIMERE simulation, and $\delta_{i,j}$ is the transfer coefficient. This transfer coefficient is derived as follows:

- $\delta_{i,j} = 0$ if the i th size bin from the initial and boundary condition datasets is found to be wholly outside the j th size bin in the CHIMERE simulation;

- $\delta_{i,j} = 1$ if the i th size bin from the initial and boundary condition datasets is wholly encompassed by the j th size bin in the CHIMERE simulation;
- $\delta_{i,j} = \frac{\log(r_{j,\max}) - \log(r_{j,\min})}{\log(R_{i,\max}) - \log(R_{i,\min})}$ if the i th size bin from the initial and boundary condition datasets wholly encompasses the j th size bin in the CHIMERE simulation;
- $\delta_{i,j} = \frac{\log(R_{i,\max}) - \log(r_{j,\min})}{\log(R_{i,\max}) - \log(R_{i,\min})}$ if the i th size bin from the initial and boundary condition datasets partially overlaps the j th size bin in the CHIMERE simulation but extends below the start of this size bin;
- $\delta_{i,j} = \frac{\log(r_{j,\max}) - \log(R_{i,\min})}{\log(R_{i,\max}) - \log(R_{i,\min})}$ if the i th size bin from the initial and boundary condition datasets partially overlaps the j th size bin in the CHIMERE simulation but extends beyond the end of this size bin.

Here $R_{i,\min}$ and $R_{i,\max}$ are, respectively, the radius of the lower and upper limit of the i th size bin from the initial and boundary condition datasets, and $r_{j,\min}$ and $r_{j,\max}$ are, respectively, the radius of the lower and upper limit of the j th size bin in the CHIMERE simulation.

For the sake of simplicity, throughout this article we will refer to the WRF–CHIMERE simulations run with the

GOCART, MERRA-2, and CAMS dust aerosol initial and boundary conditions as the “wrf_chimere-G”, “wrf_chimere-M”, and “wrf_chimere-C” simulations, respectively.

Table 2 summarises the characteristics of the three dust aerosol datasets and their associated size distributions.

2.3 Modelling strategy

The domain of simulation extends from 2 to 35° N and from 19° W to 24° E, as illustrated by the red box in Fig. 1b. The domain is large enough to represent the primary atmospheric flows, including the Harmattan north/northwest flow and the monsoon south flow, as well as the transport of the emitted aerosol plumes. A horizontal resolution of 9 km has been selected in order to ensure that the grid ratio is approximately 3 with the ERA5 meteorological forcing. This choice is also motivated by the a priori intention to achieve a resolution higher than that of previous CHIMERE simulations performed in this region, as well as to surpass the resolution of the operational solar forecast model used for the Zagtouli solar farm, which is based on global forecasting models (see Sect. 2.4.1). The CHIMERE model is configured in a “dust only” model, which models only the mineral dust type. This hypothesis is supported for this dust case study by Fig. S2 as desert dust is the dominant aerosol during the event, particularly above 10° N. This hypothesis is also reinforced by the dust optical depth (DOD) to AOD ratio derived from the CAMS reanalysis, which exceeds 80 % during this case study and for the domain of interest (not shown). It is notable that biomass burning, which represents the other principal aerosol source in this region, is no longer a significant contributor to aerosol levels at that time of the year (Evans et al., 2018).

The WRF and CHIMERE models are coupled online through the OASIS3-MCT coupler. A two-way coupling strategy is selected in which WRF sends meteorological variables to CHIMERE which in turn exchanges aerosol information such as AOD, single-scattering albedo (SSA), and the asymmetry factor. This coupling strategy imposes most of the WRF parameterisations. The exchange frequency is set to 15 min. The WRF model computes fields on 50 levels, which are linearly interpolated over the 30 CHIMERE vertical levels via the OASIS coupler. The coupling includes the feedback of aerosol–radiation interactions (ARIs; direct aerosol effect) and aerosol–cloud interactions (ACIs; indirect aerosol effects) simultaneously.

The simulation starts on 14 March 2021 at 00:00 UTC and ends on 2 April 2021 at 00:00 UTC. The first 2 weeks served as the spin-up period. The simulation outputs are analysed for the period from 28 March 2021 at 00:00 UTC to 2 April 2021 at 00:00 UTC, which corresponds to the passage of the dust plume in the Sahel region, in particular around the Zagtouli solar farm in Burkina Faso. Four simulations were conducted, namely a meteorological simulation, using WRF model alone, and dust simulations with the coupled WRF–CHIMERE models, using as initial and boundary conditions

the GOCART climatology, the MERRA-2 reanalysis, and the CAMS reanalysis. The simulation using only WRF allows for the evaluation of the impact of taking into account dust aerosols in estimating solar irradiance. This is compared to the other three simulations, which are also used to evaluate the uncertainties associated with the choice of the aerosol initial and boundary condition datasets. A domain of interest, spanning 10 to 25° N (Fig. 1a), was selected for analysis and comparisons. This choice was guided by the dust plume trajectory (Fig. S1) and the “dust-only” hypothesis (Fig. S2).

2.4 Evaluation datasets

This section presents the local and regional data that are employed in the evaluation of the simulations.

2.4.1 GHI

The global horizontal irradiance (GHI) is the total shortwave irradiance from the Sun on a horizontal surface on Earth. It is the sum of direct irradiance, which takes into account the solar zenith angle and diffuse horizontal irradiance. It is measured in W m^{-2} for the wavelength range 0.3–3.0 μm .

The national electricity company of Burkina Faso, Sonabel, operates a solar farm in Zagtouli (12.31° N, 1.64° W; Fig. 1a), approximately 15 km west of the capital, Ouagadougou. It has an installed capacity of 34 MWp and contributes up to 4 % of Burkina Faso’s annual electricity production. Ground GHI measurements from pyranometers are available at a temporal resolution of 15 min for the Zagtouli solar plant and undergo pre-processing to ensure quality control. This involves removing outliers and days with missing data, visually checking the consistency of the measured values, and selecting data corresponding to production hours (positive values for solar irradiance at the top of the atmosphere). Operational GHI forecasts for this solar farm are computed by the French company Steadysun. These forecasts are based on a multi-model, multi-member, and multi-mesh grid aggregation, which is derived from the National Centers for Environmental Prediction (NCEP) Global Ensemble Forecast System and the ECMWF Integrated Forecast System (Clauzel et al., 2024).

In situ measurements of GHI from pyranometers (Fig. 1a) are also available at a 15 min temporal resolution for the Banizoumbou (Niger) surface station, installed as part of the AMMA-CATCH observatory (African Monsoon Multidisciplinary Analysis – Coupling the Tropical Atmosphere and the Hydrological Cycle; AMMA-CATCH, 1990; Galle et al., 2018).

The two measurement sites were selected because they are the only locations where GHI observations have been made available along the dust plume transport for the case study, with the Zagtouli power station being one of the first large solar farms in West Africa and the AMMA-CATCH obser-

Table 2. Summary of the characteristics of the dust initial and boundary condition products.

	GOCART	MERRA-2	CAMS
Type	Climatology	Reanalysis	Reanalysis
Temporal resolution	Monthly	3 h	3 h
Vertical levels	20	72	60
Horizontal resolution (lat × long)	2° × 2.5°	0.5° × 0.635°	0.75° × 0.75°
Dust aerosol size distribution (radius in μm)	0.20–0.36 μm 0.36–0.60 μm 0.60–1.20 μm 1.20–2.00 μm 2.00–3.60 μm 3.60–6.00 μm 6.00–12.00 μm	0.1–1.0 μm 1.0–1.8 μm 1.8–3.0 μm 3.0–6.0 μm 6.0–10.0 μm	0.03–0.55 μm 0.55–0.90 μm 0.90–20.00 μm

vatory being the only one to offer continuous GHI measurements for the region and period of interest.

The CAMS gridded solar radiation dataset (CAMS solar radiation services v4.6; Schroedter-Homscheidt et al., 2022), based on the Heliosat-4 method (Qu et al., 2017), provides several variables related to solar irradiance, such as clear-sky and all-sky GHI. It has a horizontal resolution of $0.1^\circ \times 0.1^\circ$ and provides data every 15 min. The clear-sky model includes aerosols through the CAMS chemical transport model (Inness et al., 2019), which integrates data assimilation of AOD and is coupled online to a numerical weather prediction model. Cloud information for the all-sky model is derived from Meteosat Second Generation (MSG) satellite observations using the AVHRR Processing scheme Over cLOUDs, Land and Ocean (APOLLO) next-generation cloud processing scheme (Klüser et al., 2015). The dataset was selected for comparison with the simulations as it integrates a description of aerosol processes. While Yang and Bright (2020) and Sawadogo et al. (2023) show that it is the best-performing product for estimating surface solar irradiance in the West African region among several satellite-based gridded irradiance products, this dataset still has a negative bias of about 10 % for all-sky solar irradiance estimates at desert stations in North Africa (CAMS solar radiation regular validation report; Lefèvre, 2022).

2.4.2 Surface temperature

In situ surface temperature measurements are available for three stations of the International Network to study Deposition and Atmospheric composition in Africa (INDAAF), namely Banizoumbou (Niger; 13.54°N , 2.66°E ; 6.2 m above surface; Rajot et al., 2010a; Marticorena et al., 2010; Kaly et al., 2015), Cinzana (Mali; 13.28°N , 5.93°W ; 2 m above surface; Rajot et al., 2010b; Marticorena et al., 2010; Kaly et al., 2015), and Bambey (Senegal; 14.70°N , 16.47°W ; 5.2 m above surface; Marticorena et al., 2021a) (Fig. 1b). The mea-

surement sites were selected since they are almost aligned around $13\text{--}15^\circ \text{N}$, which represents the main pathway of Saharan and Sahelian dust towards the Atlantic Ocean during the case study.

The ERA5 atmospheric reanalysis (Hersbach et al., 2020) provides spatially continuous hourly values of surface temperature at 2 m and has a horizontal resolution of $0.25^\circ \times 0.25^\circ$.

2.4.3 Aerosol

The INDAAF network also provides data on aerosol concentration through ground measurements of PM_{10} , i.e. the concentration of atmospheric particles with an aerodynamic diameter smaller than $10 \mu\text{m}$. For this case study, hourly PM_{10} measurements are available for two stations (Fig. 1b), namely Cinzana (Rajot et al., 2010c; Kaly et al., 2015) and Bambey (Marticorena et al., 2021b).

The CAMS atmospheric reanalysis (Inness et al., 2019) is also used to evaluate regional surface PM_{10} concentration and AOD. It provides 3 h data with a horizontal resolution of $0.75^\circ \times 0.75^\circ$ and a surface layer thickness of 2.4 hPa.

Local ground measurements of AOD are retrieved from the AEROSOL ROBOTIC NETWORK level 1.5 dataset (AERONET; Holben et al., 1998; Giles et al., 2019). AOD is calculated from sun photometer recordings, along with the Ångström Exponent, and is only available during clear-sky conditions in daylight hours with a resolution of 1 min. The AOD at 400 nm simulated with the WRF-CHIMERE model is converted to 440 nm for comparison with AERONET, using the Ångström formula as follows:

$$\frac{\text{AOD}_\lambda}{\text{AOD}_{\lambda_0}} = \left(\frac{\lambda}{\lambda_0} \right)^{-\alpha}, \quad (2)$$

where AOD_λ is the AOD at the desired wavelength, which is $\lambda = 440 \text{ nm}$ here; AOD_{λ_0} is the AOD at the wavelength simulated in the model, which is $\lambda_0 = 400 \text{ nm}$ here; and α is

the Ångström exponent derived from the simulated AOD at different wavelengths and given here for the range from 400 to 600 nm.

AERONET also provides an aerosol size distribution dataset estimated through the inversion of the photometer data, as described in Dubovik and King (2000). The algorithm for inversion provides a volume particle size distribution for 22 bins, which are logarithmically distributed for radii between 0.05 and 15 μm . For comparison with the modelled aerosol size distribution, this distribution is interpolated on the CHIMERE-simulated aerosol size distribution which is composed of 10 bins ranging from 0.01 to 40.00 μm in diameter (see Table 1). Given that the coarsest bin (10.00–40.00 μm) is at the limit of the capabilities of the inversion method, and the two thinnest bins (0.010–0.022 and 0.022–0.048 μm) are out of the range of the inversion product, the AERONET dataset size sections are interpolated on the CHIMERE size sections ranging from 0.048 to 10.0 μm . Consequently, only comparisons between the three simulations can be made for the three size sections which are out of the range of the AERONET product. The column aerosol volume size distribution simulated by the model is calculated for each bin “ i ” as in Menut et al. (2016):

$$\frac{dV(r_i)}{d\ln(r_i)} = \sum_{k=1}^{n \text{ levels}} \frac{m_{k,r_i} \times \Delta z_k}{\rho_{\text{dust}} \times \ln(r_{i,\text{max}}/r_{i,\text{min}})}, \quad (3)$$

where r_i is the mean mass median radius (in μm), and $r_{i,\text{min}}$ and $r_{i,\text{max}}$ are the boundaries of the i th bin. m_{k,r_i} is the dust aerosol mass concentration (the mass of aerosol in 1 m^{-3} of air; given in $\mu\text{g m}^{-3}$). ρ_{dust} is the dust aerosol density (the mass of the particle in its own volume; $\rho_{\text{dust}} = 2300 \text{ kg m}^{-3}$). Δz_k is the model layer thickness (in metres) for a total of n levels (here 30 vertical levels).

The locations of the five AERONET sites used for comparison in this study are illustrated in Fig. 1a.

The spatially continuous AOD is also derived from level 2 aerosol products of MODIS Terra and Aqua satellites (combined Dark Target–Deep Blue AOD at 0.55 μm , Collection 6.1; Platnick et al., 2015). It provides a measure of the AOD at 550 nm during the daytime for clear-sky conditions, with a spatial resolution of 10 km. To compare simulated AOD from WRF–CHIMERE models with AOD from MODIS, the former is converted from 600 to 550 nm. The conversion is performed using the Ångström formula (Eq. 2).

Table 3 provides a general overview of the data used to evaluate the simulations in this study.

3 Results

The analysis starts by assessing the errors and uncertainties associated with the dust aerosol initial and boundary condition datasets employed to estimate the variables of interest for solar production, i.e. GHI and surface temperature. Subsequently, we investigate the potential causes of these uncertainties by evaluating the AOD, aerosol size distribution, and

surface aerosol concentration (PM_{10}), as well as by examining mineral dust emissions and the flux of these aerosols at the boundaries of the domain. The metrics used to assess the quality of the simulations are described in the Supplement.

3.1 GHI

In Fig. 2, the local evaluation demonstrates the effect of taking into account dust aerosol for GHI estimation with the WRF–CHIMERE coupling over the WRF meteorological model alone. The coupling reduces the MAE by a factor of 3.6 at Zagtouli and by a factor of 4.6 at Banizoumbou on average. The simulations accurately represent the reduction in GHI intensity caused by the dust plume at both stations. However, the reduction persists compared to the observations at Zagtouli. At Banizoumbou, the simulations overestimate GHI at the beginning and end of the case study.

Figure 2 also indicates that the CAMS gridded solar radiation product fails to fully reproduce the dust event, with only a small reduction in GHI during the passage of the dust plume and an intermediate MAE between the WRF-only and the WRF–CHIMERE simulations. This point serves to highlight the advantages of using a regional model in comparison to a global product for the simulation of dust conditions and the estimation of solar irradiance.

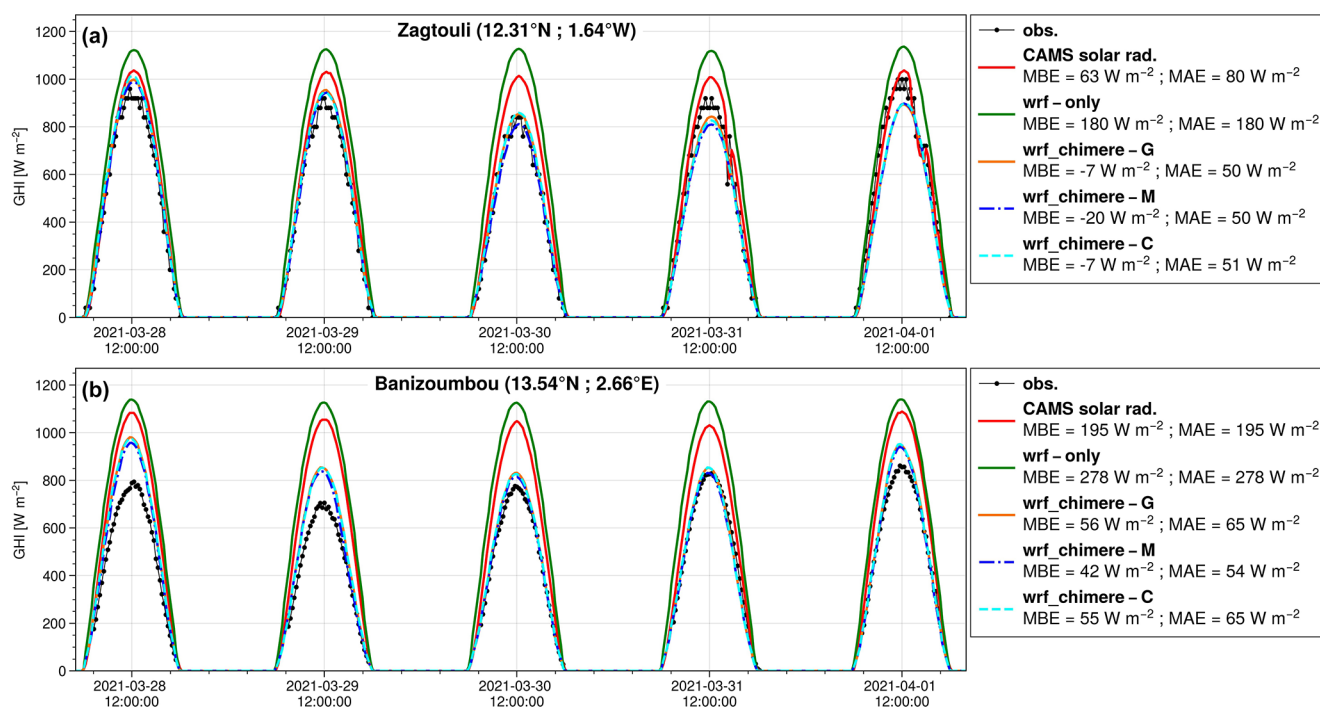
Furthermore, the uncertainty in GHI estimation related to the choice of the dust aerosol initial and boundary condition datasets is limited, particularly when compared to the errors. This is evidenced by the fact that the mean standard deviation between the three WRF simulations is only 7 % of the average MAE of these simulations at Zagtouli and only 5 % at Banizoumbou.

The regional comparison presented in Fig. 3 provides more insight into the impact of incorporating dust on GHI estimation with the WRF–CHIMERE coupling when compared to the WRF meteorological model alone. As anticipated, the WRF-only simulation has the highest GHI estimates. The WRF–CHIMERE simulations indicate that dust aerosols reduce the mean GHI estimation by approximately 115 W m^{-2} (–18 %) compared to the WRF-only simulation, while the CAMS gridded solar radiation global product shows a reduction of 88 W m^{-2} (–14 %). The three WRF–CHIMERE simulations exhibit identical regional patterns, with lower mean GHI values observed on the dust plume trajectory from the Bodélé Depression to the west and also in the south Atlas region. In contrast, the CAMS gridded solar radiation dataset does not show this regional pattern, which may indicate that this global product does not fully capture the dust event.

Furthermore, the uncertainty in GHI estimation associated with the choice of the dust aerosol initial and boundary condition datasets is limited, particularly when compared to the changes brought by the taking of dust aerosol into account. Indeed, the standard deviation between the three WRF–CHIMERE simulations represents only 5 % of

Table 3. Summary of data used to evaluate the simulations.

	Product	Type	Resolution
GHI	Zagtouli solar farm monitoring system	Pyranometer GHI measurement	Local
	AMMA-CATCH observational network	Pyranometer GHI measurement	Local
	CAMS gridded solar radiation	Atmospheric reanalysis	$0.01^\circ \times 0.01^\circ$
Temperature	INDAAF network	Ground measurements	Local
	ERA5	Atmospheric reanalysis	$0.25^\circ \times 0.25^\circ$
PM ₁₀	INDAAF network	Ground measurements	Local
	CAMS (v48R1, EAC4)	Atmospheric reanalysis	$0.75^\circ \times 0.75^\circ$
Aerosol size distribution	AERONET network	Inversion product	Local
Aerosol optical depth	AERONET network	Sun photometer ground measurements	Local
	MODIS	Satellite observations	10 km

**Figure 2.** Local comparison of CAMS gridded solar radiation product and simulated GHI against (a) the Zagtouli solar farm observations and (b) the Banizoumbou AMMA-CATCH observations. wrf_chimere-G, wrf_chimere-M, and wrf_chimere-C refer to the WRF-CHIMERE simulations using GOCART, MERRA-2, and CAMS as dust aerosol initial and boundary condition datasets, respectively.

the mean difference between these three simulations and the WRF-only simulation without dust.

3.2 Temperature

Figure 4 illustrates the contrasting outcomes of taking into account dust aerosols into the WRF-CHIMERE coupling in comparison to the WRF meteorological model alone for the estimation of surface temperature. At Bambey (Fig. 4a), which is far from the dust source areas, the coupling has no effect on daytime temperatures but does affect nighttime

temperatures. The WRF-CHIMERE and WRF-only simulations have indicator of agreement (IOA) and mean absolute error (MAE) of the same order of magnitude. At Cinzana (Fig. 4b), the WRF-only simulation performed better, with an MAE 0.6 °C lower than the coupled simulations, especially for nighttime temperatures but also for estimating the daily temperature peak. Finally, at Banizoumbou (Fig. 4c), which is near the dust source areas, the coupling leads to a significant improvement in surface temperature estimation, with an IOA of approximately 0.79 compared to 0.56 for the WRF-only simulation and an MAE reduced by around

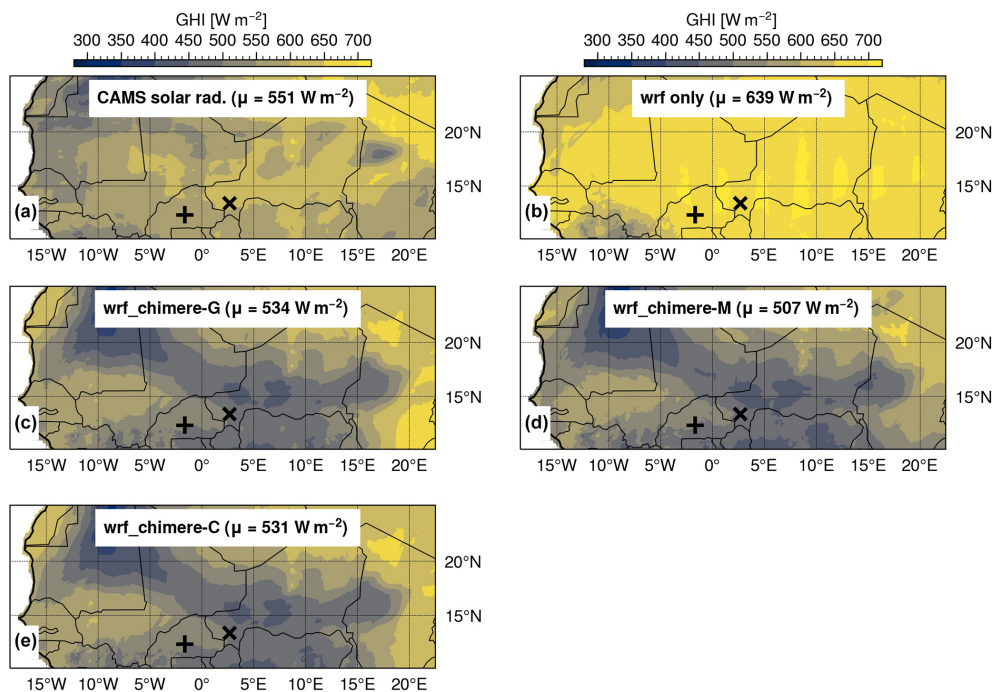


Figure 3. Mean daytime GHI during the period of 28 March 2021 at 00:00 UTC to 2 April 2021 at 00:00 UTC as estimated by (a) the CAMS gridded solar radiation dataset, (b) the WRF only simulation, and the WRF–CHIMERE simulations with (c) GOCART, (d) MERRA-2, and (e) CAMS as dust aerosol initial and boundary condition datasets; the plus sign (+) is the Zagtouli solar farm, and the cross (x) is the Banizoumbou site. μ is the mean GHI estimates over the domain.

3.6 °C. The impact of dust aerosols on temperature is particularly pronounced at nighttime. However, dust also affects the daily temperature peak, with a reduction of 1.1 °C of the daily maximum temperature observed on 30 March.

Depending on the position of the measurement station, the results show a contrast. There is a significant improvement in the model coupling close to the source zones at Banizoumbou. However, this improvement is reversed with increasing distance at Cinzana. This suggests errors in the simulation of the transport of the dust plume from the source zones (Bodélé Depression) towards the west. Overall, the main differences between WRF only and WRF–CHIMERE coupled simulations occur at nighttime when there is no solar production. These differences highlight the warming effect due to the dust aerosol interaction with the longwave earth radiation.

In general, the uncertainty associated with the choice of the dust aerosol initial and boundary condition datasets for the WRF–CHIMERE simulations is negligible compared to the errors in temperature estimation or the difference with the WRF-only simulation.

The value of the ERA5 reanalysis for surface temperature evaluation is also reinforced in Fig. 4 since it shows the lowest MAE and highest IOA. This dataset can therefore be considered reliable for a regional evaluation of surface temperature.

The regional surface temperature evaluation in Fig. 5 also reveals a contrast benefit of the coupling approach for sur-

face temperature estimation. While the WRF-only simulation (Fig. 5a) underestimates the surface temperature all over the domain, WRF–CHIMERE simulations overestimate surface temperature in the dusty areas (Saharan region; Fig. 5b, c, d). Overall, incorporating the dust aerosol simulation in the estimation of surface temperature reduces the MAE by 14 % (Fig. 5e) when comparing the surface temperature estimates from simulations with the ERA5 reanalysis.

Furthermore, the uncertainty associated with the choice of the dust aerosol initial and boundary condition datasets is limited. This is demonstrated by the fact that the standard deviation between the three WRF–CHIMERE simulations averaged over the period of the analysis is 12 % of the mean bias of those three simulations in comparison to ERA5 reanalysis and only 7 % of the difference between the coupled simulations and the WRF-only simulation without dust.

Finally, the incorporation of dust aerosol into the estimation of GHI appears to be a crucial element in this case study. However, the value of this approach is more debatable in the context of surface temperature estimation. Furthermore, the uncertainty related to the dust aerosol initial and boundary condition dataset selection is limited, particularly when compared to the simulation errors, and to the differences between including dust in the simulation and not including it. The following sections will examine the simulated dust aerosol condition during the case study in order to explain the discrep-

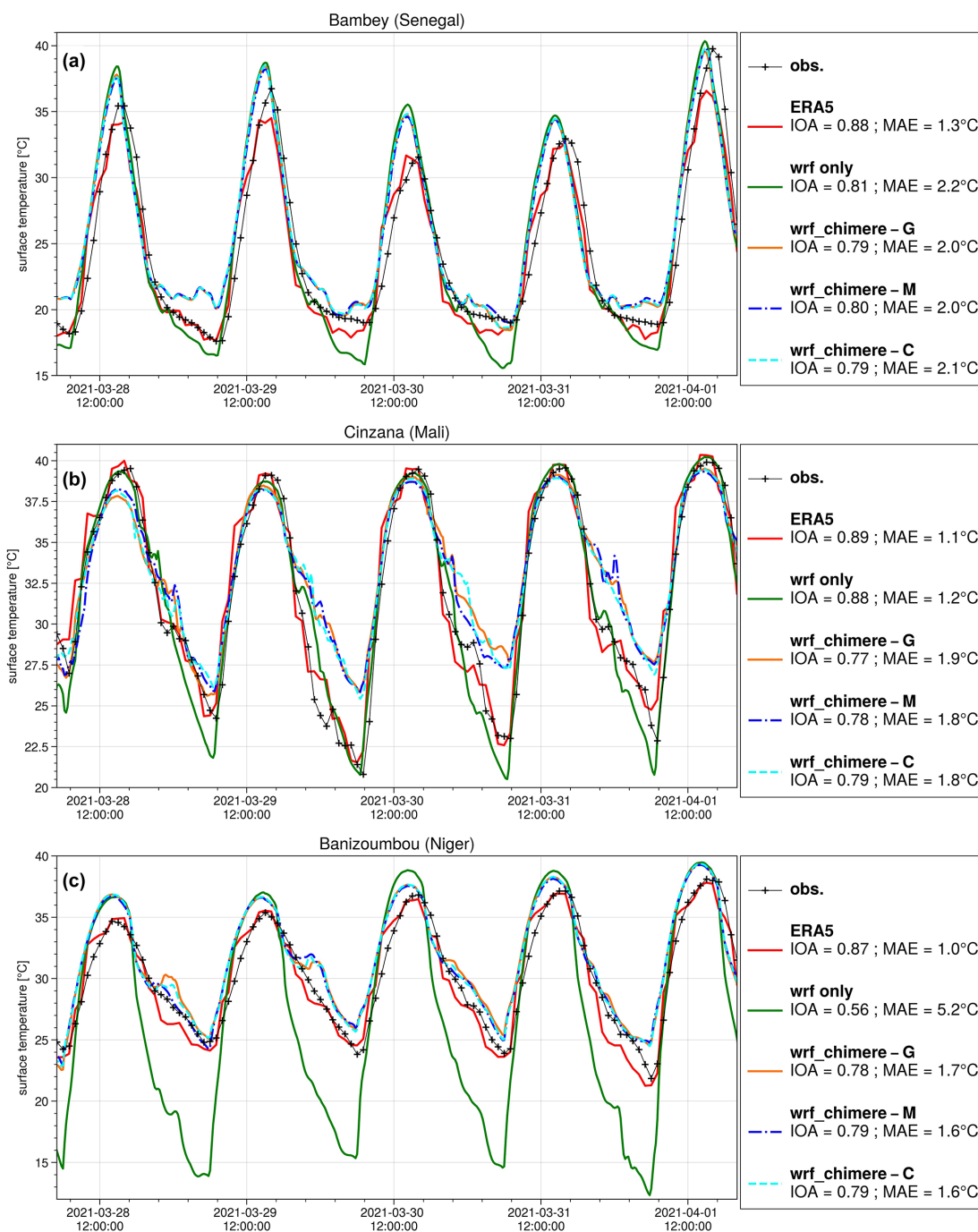


Figure 4. Local comparison of ERA5 and simulated surface temperature with the INDAAF observations for the (a) Bambe (Senegal), (b) Cinzana (Mali), and (c) Banizoumbou (Niger) measurement sites. wrf_chimere-G, wrf_chimere-M, and wrf_chimere-C refer to the WRF-CHIMERE simulations using GOCART, MERRA-2, and CAMS as dust aerosol initial and boundary condition datasets, respectively. IOA is the indicator of agreement, and MAE is the mean absolute error.

ancies observed in GHI and surface temperature, which are key parameters for solar production.

3.3 Aerosol optical depth

The local evaluations presented in Fig. 6 reveal an overestimation of the AOD for stations close to dust sources such as Tamanrasset (Fig. 6a), Zinder (Fig. 6b), and Banizoumbou (Fig. 6c). This overestimation is more limited with in-

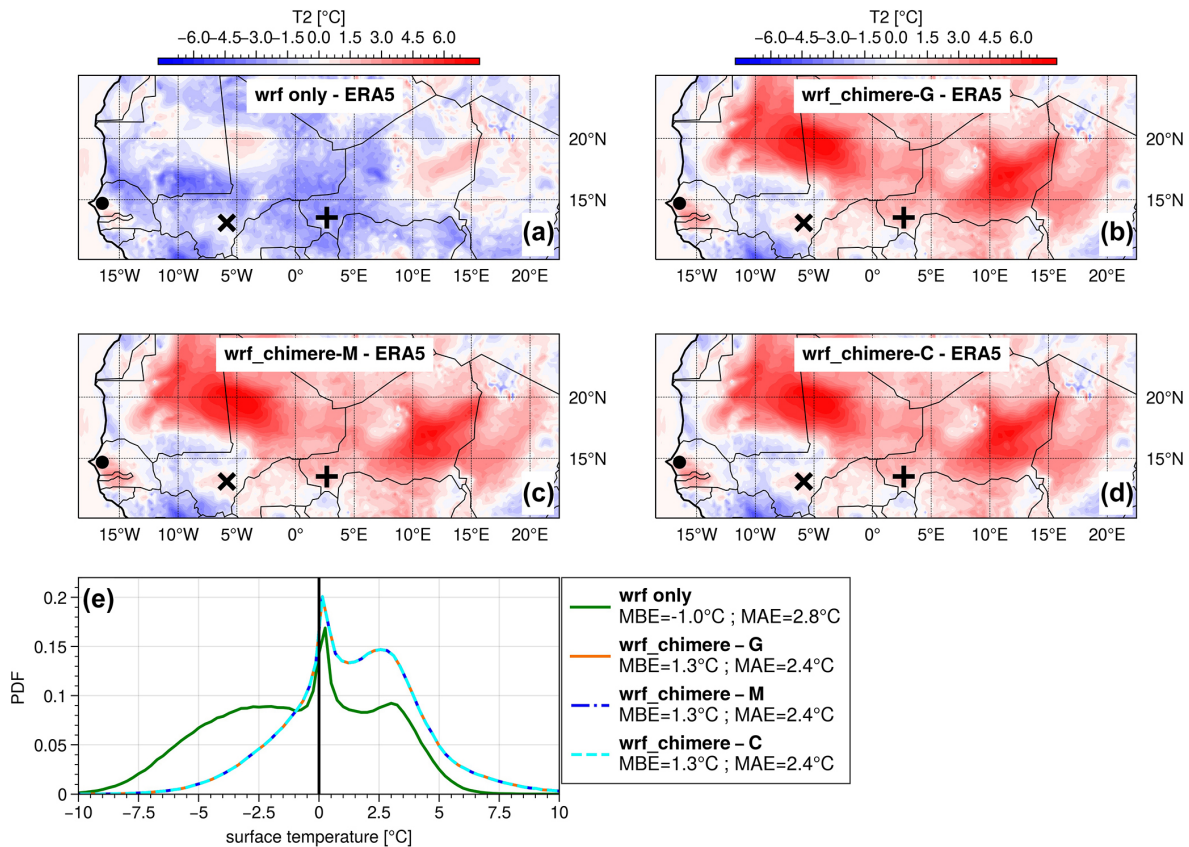


Figure 5. Mean difference in surface temperature compared to the ERA5 reanalysis for (a) the WRF-only simulation and the WRF-CHIMERE simulations with (b) GOCART, (c) MERRA-2, and (d) CAMS as dust aerosol initial and boundary condition datasets during the period of 28 March 2021 at 00:00 UTC to 2 April 2021 at 00:00 UTC. The black point is Bambey, the cross (×) is the site at Cinzana, and the plus sign (+) is the Banizoumbou INDAAF site. (e) Probability density function for the differences in surface temperature between simulations and the ERA5 reanalysis.

creasing distance from the dust source at Cinzana (Fig. 6d) and Dakar (Fig. 6e). The order of magnitude of the dispersion between the three simulations is small when compared to the errors in the simulation in representing the observed AOD. As a consequence, the uncertainty associated with the choice of the dust aerosol initial and boundary condition datasets is limited. Overall, the AERONET AOD measurements appear to be very scarce, particularly close to the dust aerosol sources (Zinder, Tamanrasset, Banizoumbou, and Cinzana). The AOD measurements are performed by sun photometers which provide recordings by pointing at the Sun. Thus, these recordings are only available during the daytime and with clear-sky conditions. In some cases of intense dust plumes with very high concentrations leading to strong solar radiation absorption, the sun photometers are technically limited and cannot produce any record or, sometimes, the AERONET quality control system removes them (Mueller et al., 2015; Giles et al., 2019). This may be the reason for the scarcity of observations in this case study which focuses on an intense dust event, thus increasing the perceived overestimation of the simulations. To compensate for

this, the AOD estimates from MODIS satellite observations have been added to Fig. 6 to complete the data.

Furthermore, the CAMS reanalysis appears to be a reliable dataset for dust AOD estimation as it has no overestimation and has the lowest normalised mean absolute error (nMAE) for all sites. Although it does not reproduce the AOD dynamics close to the dust source at Tamanrasset and Zinder, it has the highest correlation coefficient for the other sites. Nevertheless, this result should be interpreted with caution, given the limited data available for calculating the dataset evaluation metrics. More research is needed to substantiate this conclusion.

The AOD differences shown in Fig. 7b, c, and d show that the simulations significantly overestimate the AOD compared to the MODIS satellite observations, particularly in the Saharan and north Sahelian zones and in the south Atlas, with an average overestimation of +1.25 between 15 and 20° N. It is important to note that this overestimation is localised close to the desert aerosol source zones. The simulated AOD error in the Sahel zone, particularly around the Zagtouli solar power plant, is more limited, with an average of +0.51 be-

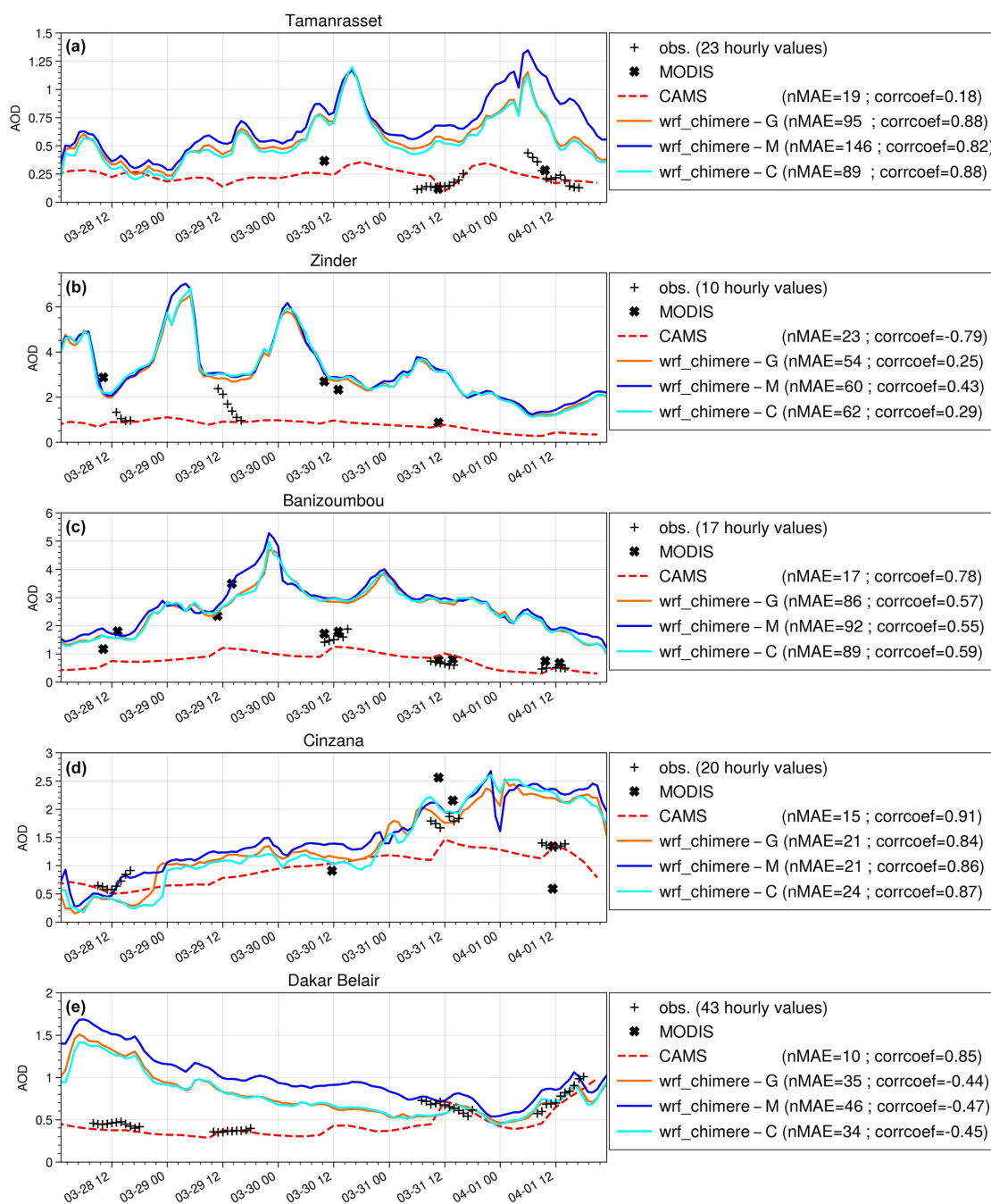


Figure 6. Local comparison of simulated AOD with AERONET in situ measurements at 440 nm for (a) Tamanrasset, (b) Zinder, (c) Banizoumbou, (d) Cinzana, and (e) Dakar Belair stations. wrf_chimere-G, wrf_chimere-M, and wrf_chimere-C refer to the WRF-CHIMERE simulations using GOCART, MERRA-2, and CAMS as dust aerosol initial and boundary condition datasets, respectively. MODIS and CAMS refer to the AOD at 440 nm from the MODIS satellite observations and the CAMS atmospheric reanalysis, respectively. nMAE is the normalised mean absolute error in percent, and corrcoeff is the Person correlation coefficient. Both are derived with AERONET measurements as the reference.

tween 10 and 15°N. The mean standard deviation between the three WRF-CHIMERE simulations is only 10% of the mean error and 5% of the mean simulated AOD. Consequently, the uncertainty in the AOD estimate associated with

the selection of the dust aerosol initial and boundary condition datasets is small.

The observed overestimation of AOD by the WRF-CHIMERE simulations could be due to an overestimation of the aerosol concentration, an inaccurate estimation of the size

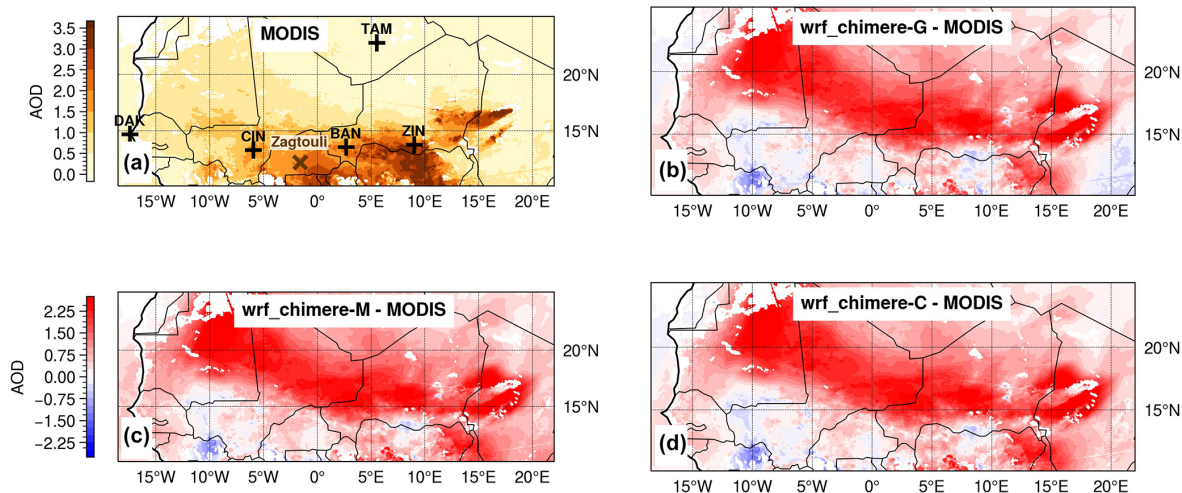


Figure 7. (a) Mean from 28 March 2021 at 00:00 UTC to 2 April 2021 at 00:00 UTC of MODIS AOD at 550 nm satellite observations. The cross (×) is the Zagtoui solar farm, and the plus sign (+) corresponds to the AERONET station. For panels (b), (c), and (d), AOD at 550 nm mean differences from 28 March 2021 at 00:00 UTC to 2 April 2021 at 00:00 UTC between each of the WRF–CHIMERE simulations are driven by GOCART, MERRA-2, and CAMS, respectively, and the MODIS satellite observations.

distribution of the dust plume, excessive aerosol emissions within the domain, or an excessive inflow of desert aerosols at the domain boundaries. These hypotheses are investigated below. Another potential explanation may also be the uncertainties in the radiative properties of the dust aerosol incorporated in the CHIMERE model or an underestimation of the aerosol deposition flux; these aspects are not investigated here.

3.4 Aerosol size distribution

The evaluation of the aerosol size distribution in Fig. 8 shows that the simulations generally have a dominant aerosol size mode shifted towards coarser sizes compared to the AERONET inversion product. The ground-based size distribution has a strong peak between 1.14 and 5.00 μm , whereas the size distributions estimated by the WRF–CHIMERE simulations peak for coarser aerosol. For the Dakar Belair station (Fig. 8d), the AERONET inversion product indicates a first peak of lower intensity between 0.05 and 0.11 μm , which suggests the presence of aerosols other than desert dust. These aerosols may be of anthropogenic origin, given the proximity of the measurement site to the Senegalese capital. When comparing the size distributions between the three simulations with different dust aerosol initial and boundary condition datasets, it can be seen that the simulations driven with CAMS and MERRA-2 reanalysis are relatively close and well separated from the one driven with the GOCART climatology. Notably, the dominant size bin in the simulation using GOCART dataset is consistently the one with the largest particles, whereas with the aerosol from reanalyses it is the aerosols between 5 and 10 μm . Consequently, the uncertainty associated with the selection of the dust aerosol

initial and boundary condition datasets is high when examining the aerosol size distribution, particularly for particles exceeding 5.00 μm in diameter. The aforementioned uncertainties in the aerosol size distribution, which are linked to the choice of the dust aerosol initial and boundary condition datasets, may be attributed to differences in the flow of desert dust entering the domain, as well as uncertainties in the transfer method carried out by the CHIMERE model to match the aerosol classes of these datasets to its own size distribution as described in Sect. 2.2.3.

As a result, the shift in the WRF–CHIMERE size distribution towards coarser particles compared to AERONET observations would result in a simulated AOD smaller than AERONET measurements. However, the opposite is observed (Sect. 3.3). This suggests a positive bias in the simulated aerosol concentration, which would explain the positive bias in the AOD, while the coarser size distribution would tend to compensate.

3.5 Aerosol concentrations

The three simulations properly capture the dynamics of the PM_{10} surface concentration with respect to the INDAAF ground measurement (Fig. 9) as correlation coefficients are around 0.6 at Cinzana and close to 0.7 at Bambe. The WRF–CHIMERE simulations driven with MERRA-2 and CAMS dust aerosol datasets overestimate the surface PM_{10} concentration peaks for Bambe (Fig. 9a) and Cinzana (Fig. 9b), with high positive bias values of around 63 g m^{-3} at Bambe and 247 g m^{-3} at Cinzana. The latter station is closer to the dust aerosol sources. In contrast, the simulation using the GOCART dust aerosol dataset demonstrates superior performance in representing this variable, with an MAE that is

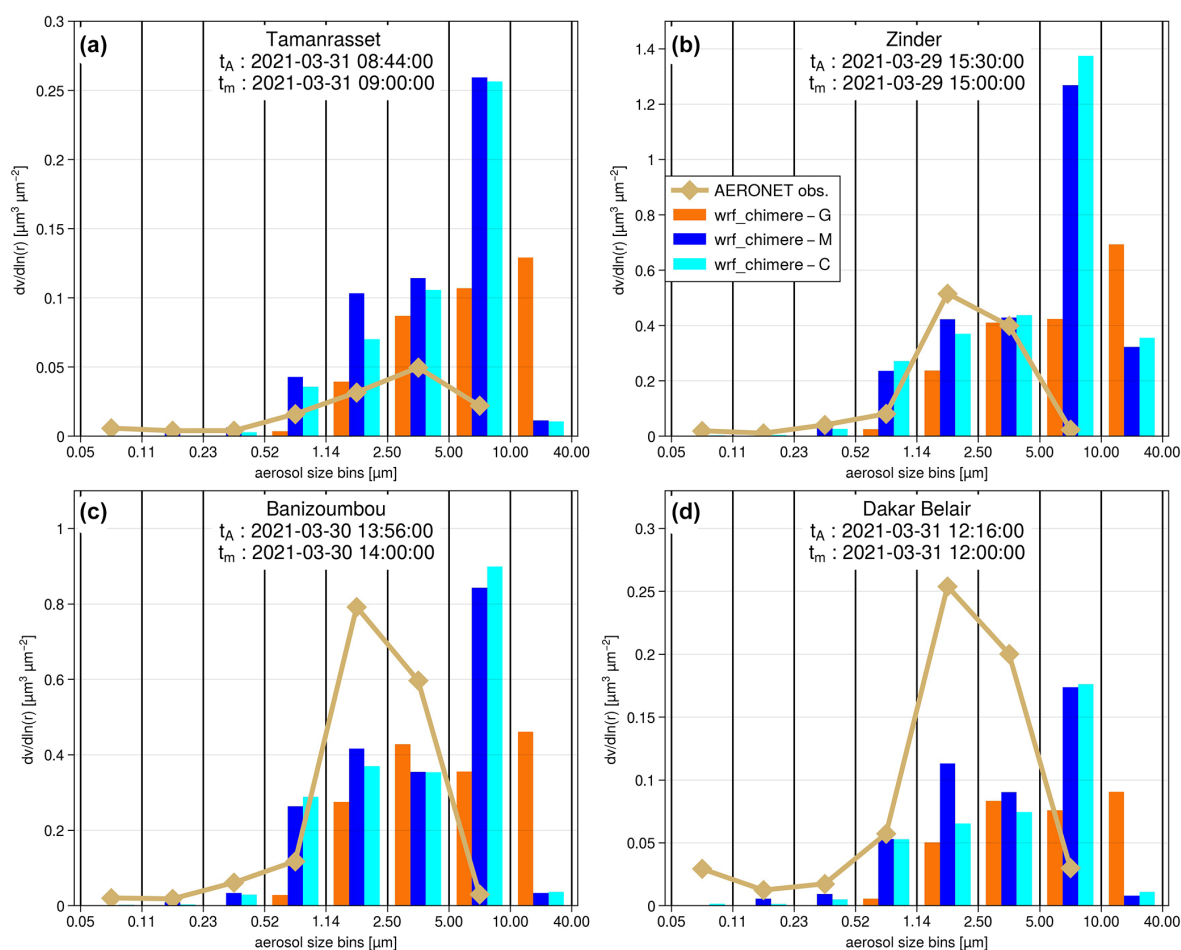


Figure 8. Aerosol volume size distribution for the AERONET station located in (a) Tamanrasset, (b) Zinder, (c) Banizoumbou, and (d) Dakar Belair. t_A and t_m indicate the times of the AERONET inversion product and the WRF-CHIMERE model, respectively, used for the comparison. wrf_chimere-G, wrf_chimere-M, and wrf_chimere-C refer to the WRF-CHIMERE simulations using GOCART, MERRA-2, and CAMS as dust aerosol initial and boundary condition datasets, respectively.

approximately 60 % and 70 % lower than the two other simulations at Bambey and Cinzana, respectively.

Furthermore, the uncertainty associated with the selection of initial and boundary condition datasets for dust aerosols is of a comparable magnitude to the simulation errors observed for surface PM_{10} concentrations. Section 3.4 partly explains these discrepancies in surface PM_{10} concentration estimates between the simulation driven with the GOCART climatology and those driven with CAMS or MERRA-2 reanalysis in terms of aerosol size distribution. These differences may also be attributed to variations in the size distribution of dust aerosol emissions or in the inflow of dust into the simulation domain and its aerosol size distribution.

Moreover, Fig. 9 indicates that the CAMS reanalysis provides reliable estimates of surface PM_{10} concentration, as evidenced by the fact that it has the lowest MAE values. However, the Bambey and Cinzana ground measurements, which are the only two available for the case study, are situated at a considerable distance from the dust sources, limiting our

ability to assess the accuracy of the CAMS reanalysis in capturing the dust event. Moreover, the CAMS reanalysis exhibits a negative bias at Cinzana, which is the closest site to the dust sources.

Figure 10 illustrates an overestimation of the PM_{10} concentrations compared to the CAMS reanalysis. This is particularly evident in dust source areas such as the Bodélé Depression. The WRF-CHIMERE simulation driven with the GOCART dataset is the closest to the CAMS reanalysis, with a mean estimate 3.6 times higher. However, this ratio reaches 8.6 for the simulations driven with the CAMS and MERRA-2 reanalysis dataset.

The mean standard deviation between the three WRF-CHIMERE simulations is 35 % of their mean PM_{10} surface concentration estimate. Consequently, the uncertainty in the estimation of dust PM_{10} surface concentration associated with the selection of the dust aerosol initial and boundary condition datasets is significant. The discrepancies between the simulation using the GOCART climatology and

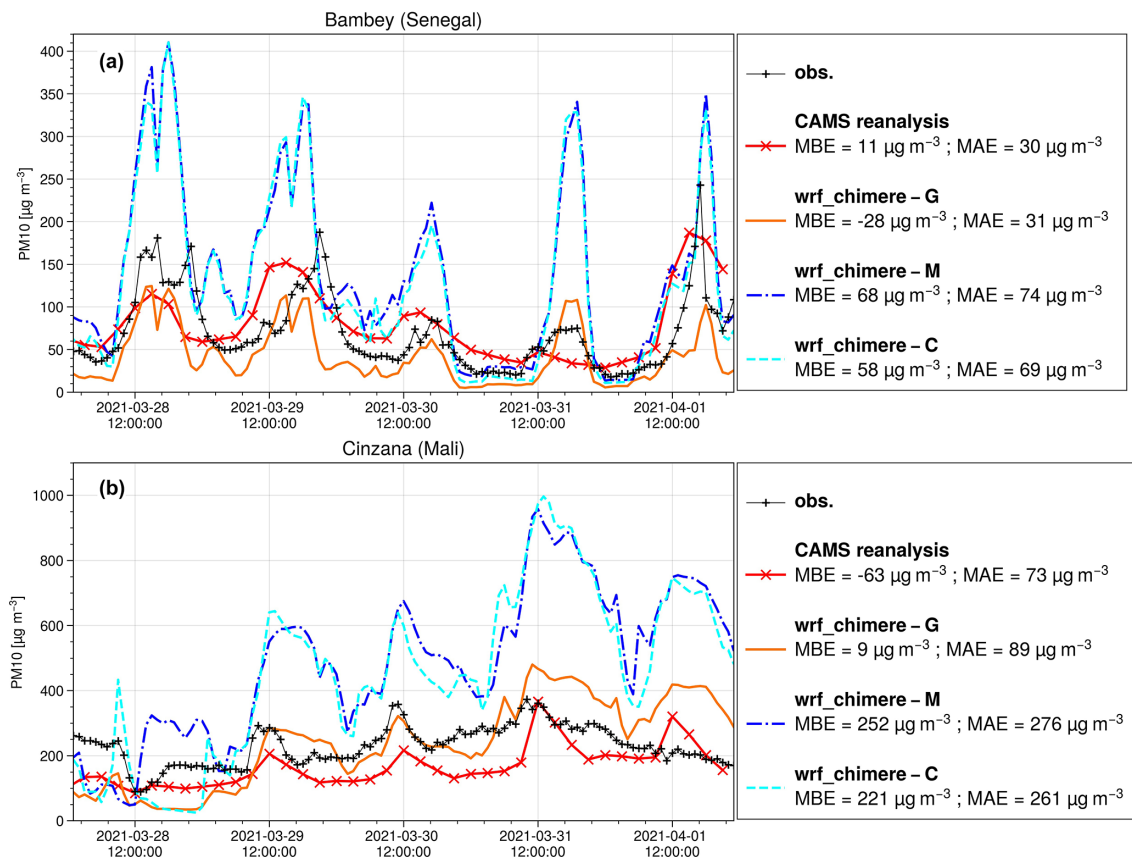


Figure 9. Local comparison of CAMS reanalysis and simulated PM_{10} surface concentrations with INDAAF network observations for (a) Cinzana and (b) Bambe stations. wrf_chimere-G, wrf_chimere-M, and wrf_chimere-C refer to the WRF-CHIMERE simulations using GOCART, MERRA-2, and CAMS as dust aerosol initial and boundary condition datasets, respectively. MBE is the mean bias error, and MAE refers to the mean absolute error.

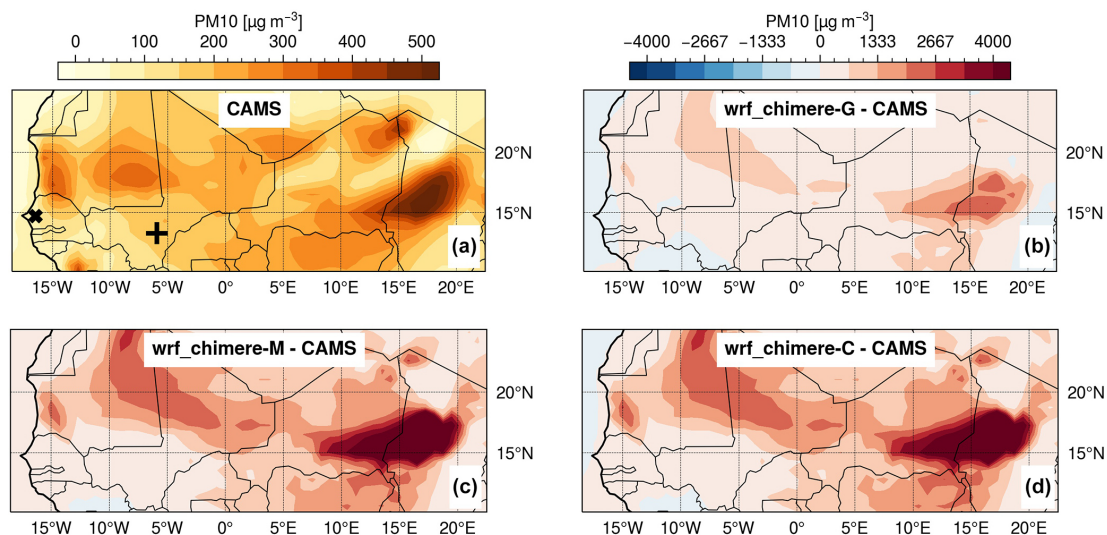


Figure 10. (a) Mean from 28 March 2021 at 00:00 UTC to 2 April 2021 at 00:00 UTC of CAMS reanalysis PM_{10} surface concentration. The cross (\times) refers to Bambe, and the plus sign (+) corresponds to the Cinzana INDAAF station. For panels (b), (c), and (d), PM_{10} surface concentration mean differences from 28 March 2021 at 00:00 UTC to 2 April 2021 at 00:00 UTC between each of the WRF-CHIMERE simulations driven by GOCART, MERRA-2, and CAMS, respectively, and the CAMS reanalysis.

the two other ones using CAMS or MERRA-2 reanalysis can be partly explained by the differences in the simulated aerosol size distribution, as shown in Sect. 3.4.

3.6 Dust emissions

In terms of dust emissions (Fig. 11), the Bodélé Depression is, as expected, identified as the primary dust source area, with emissions reaching up to 244 g m^{-2} . The differences in the simulations with each of the three dust aerosol initial and boundary condition datasets, relative to their mean, exhibit the highest values in the source zones located at the Bodélé Depression and the south Atlas. Nevertheless, it is worth noting that there is a factor of 100 in between the emissions in the Bodélé area (approximately 200 g m^{-2}) and the observed differences between the three simulations. Consequently, the uncertainties in dust emissions resulting from the choice of the dust aerosol initial and boundary condition datasets can be considered negligible. As emissions are primarily influenced by surface wind, it can be inferred that the uncertainty generated by the dust aerosol driving dataset on the surface wind is negligible too, which is confirmed by Fig. S4. Additionally, the size distributions of the aerosols emitted during the case study are found to be identical (not shown). Therefore, the differences in dust surface concentration and dust aerosol size distribution may be partly attributed to the dust flows at the boundaries of the domain and are not linked to differences in simulated dust emissions within the domain. However, there are no observational data available to enable a quantitative evaluation of the accuracy of the emissions computed within the WRF–CHIMERE simulations.

3.7 Dust boundary flux

As shown in Fig. 1b, the dust event is associated with a strong Harmattan flow that is characterised by a northeasterly flow in the lower layer. It is thus interesting to quantify the dust inflow associated with each of the dust aerosol initial and boundary condition datasets for the eastern domain boundary. The lowest dust flux is observed with GOCART (Fig. 12a), with a maximum of approximately 480 g m^{-2} . In contrast, MERRA-2 and CAMS (Fig. 14 b and c, respectively) exhibit higher dust fluxes, with maximum values of around 1650 g m^{-2} . The maximum flow is around 10° N for MERRA-2, while for CAMS it is closer to 16° N . Given that GOCART is a climatology, it is reasonable to expect a lower dust flux compared to the CAMS and MERRA-2 reanalyses, which are real-case simulations incorporating data assimilation of AOD. This is particularly true for the presented case study, which involves an intense dust event associated with a Harmattan flow.

There are also significant differences in both quantity and distribution by aerosol size bin (Fig. 12d). MERRA-2 exhibits a strong dominant mode for the class between 1.14 and $2.50 \mu\text{m}$, while CAMS shows significant values from 0.52 to

$40 \mu\text{m}$, with a maximum for the size class between 0.52 and $1.14 \mu\text{m}$. Finally, the GOCART model displays a lower variability between 1.14 and $40.00 \mu\text{m}$, with the maximum occurring for the size class between 2.55 and $5.00 \mu\text{m}$.

The eastern dust fluxes at the boundary significantly vary, depending on the dataset used as the dust aerosol initial and boundary conditions, in terms of quantity and size distribution. The reanalysis dataset, CAMS and MERRA-2, are expected to provide a more accurate representation of dust flux in terms of quantity as they are real-case simulations assimilating observational data in their calculations; this is in contrast to GOCART, which is a climatology. However, GOCART provides a more comprehensive description of aerosol size distribution with seven classes compared to CAMS, which has only three classes but proposes a higher horizontal resolution. While GOCART considers the effect of aerosol size to be essential, CAMS assumes the horizontal resolution to be a key parameter. MERRA-2 is the most comprehensive of the three datasets, with the highest horizontal resolution and an aerosol size distribution that is close to the GOCART one with five classes.

As a result, and in consideration of the negligible uncertainty in dust emissions within the simulation domain related to the choice of the dataset for dust aerosol initial and boundary conditions (see Sect. 3.6), these differences in eastern dust fluxes appear to account for the uncertainties in the simulated surface dust concentrations (see Sect. 3.5) and dust aerosol size distribution (see Sect. 3.4).

3.8 Discussions

The evaluation of the simulated GHI at the Zagtouli solar power plant and the Banizoumbou site (Fig. 2) indicates a significant enhancement in surface solar irradiance estimation when WRF is coupled with CHIMERE. Specifically, the local MAE is reduced by approximately 75 %. This confirms the relevance of incorporating the dust radiative effect with a coupling approach in comparison with the operational forecasts currently employed based on meteorological models alone. During the dry season, dust events similar to the one presented here, with emissions at Bodélé and then transport of the plume westwards, are common. This work therefore calls for forecasters in the photovoltaic sector to better account for the desert dust cycle in their forecast products. This local evaluation also highlights the potential benefits of using a regional model rather than a global product as the WRF–CHIMERE simulations outperform the CAMS gridded solar radiation product with an average MAE reduced by approximately 38 % at the Zagtouli solar farm and by 70 % at the Banizoumbou site, which is closer to dust sources. These discrepancies are corroborated by the regional comparison presented in Fig. 3, which reveals that the mean WRF–CHIMERE GHI estimate is 5 % lower than the CAMS solar radiation dataset. Additionally, the latter does not exhibit a geographical pattern with a lower GHI estimation

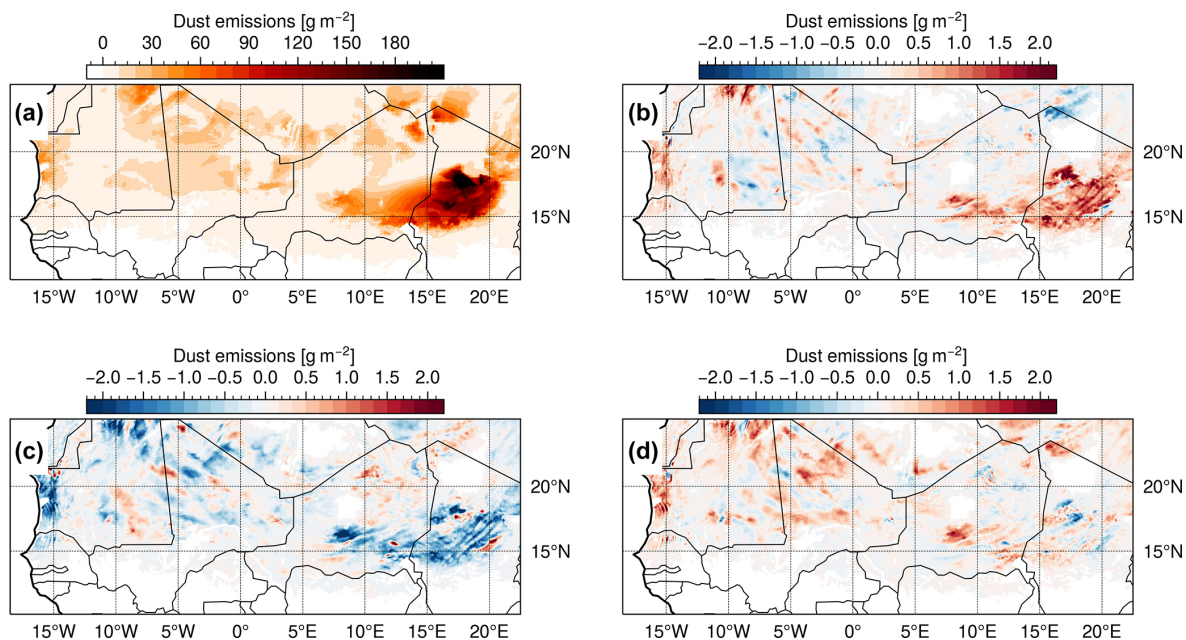


Figure 11. (a) Total dust emission flux from 28 March 2021 at 00:00 UTC to 2 April 2021 at 00:00 UTC averaged between the three WRF-CHIMERE simulations. For panels (b), (c), and (d), total dust emission individual differences between each of the WRF-CHIMERE simulations driven by GOCART, MERRA-2, and CAMS, respectively, and the mean of the three WRF-CHIMERE simulations.

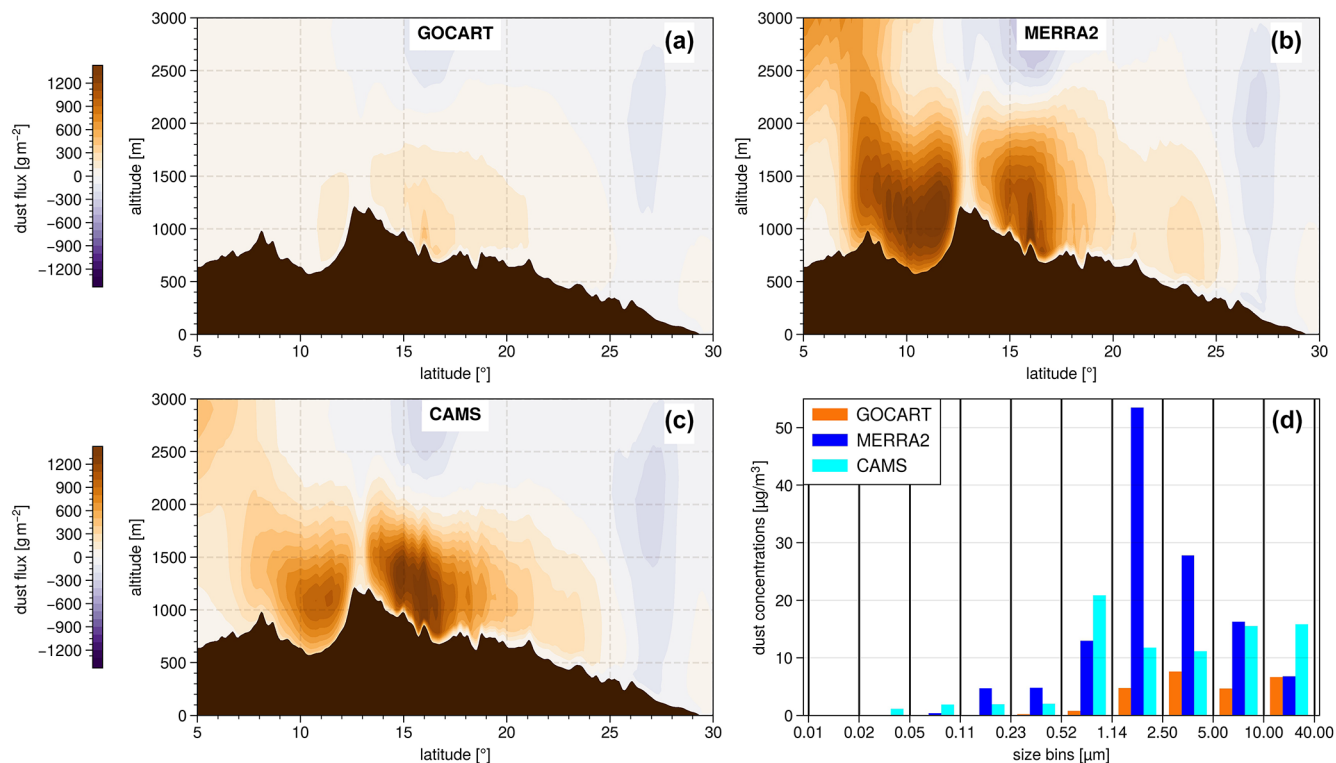


Figure 12. Cumulative dust flux at the eastern boundary of the simulation from 28 March 2021 at 00:00 UTC to 2 April 2021 at 00:00 UTC for the WRF-CHIMERE simulation with (a) GOCART, (b) MERRA-2, and (c) CAMS as dust aerosol initial and boundary condition datasets. (d) Dust size distribution at the eastern boundary limit average during the case study period from the surface to 200 hPa and over latitude. In panels (a)–(c), the dust flux is derived as the product between the dust aerosol concentration and the zonal wind, and positive values of the dust flow indicate a flow entering the simulation domain.

along the dust plume trajectory, which is in contrast to the WRF–CHIMERE simulations. These results confirm those from Sawadogo et al. (2023), who recently showed that the CAMS reanalysis has low performances in estimating solar irradiance during high AOD episodes like the one studied here. Furthermore, the comparison reveals that incorporating dust in the simulation reduces surface solar irradiance by 18 % in this case study. This reduction is notably higher but remains within the same order of magnitude as previous studies that integrated dust aerosol information for solar estimation. For example, Masoom et al. (2021) in India and Mostamandi et al. (2023) in the Arabian Peninsula reported GHI reductions due to dust of approximately 5 %–10 %. This discrepancy underscores the potential variability in the dust impact on solar irradiance, depending on the method used to account for dust effects in the simulations. In light of the anticipated expansion of PV production in West Africa, this point underscores the potential consequences of such dust events if they are not accurately predicted.

The evaluation of local surface temperature (Fig. 4) reveals contrasting results regarding the effectiveness of the coupled approach. It demonstrates an average local MAE reduction by approximately 10 % compared to the WRF-only simulation. However, the main differences occur mainly at night when no photovoltaic is produced, as previously observed by Yue et al. (2010) and Briant et al. (2017). It can be attributed to the opposing radiative forcing effects of dust aerosols across different wavelength ranges. In the case of the longwave, which corresponds to terrestrial radiation, the presence of dust aerosols has a warming effect. Conversely, for the shortwave, which corresponds to solar radiation, the presence of dust aerosols induces a cooling effect. Consequently, during nighttime when solely terrestrial radiation is present, there is an increase in surface temperature. During the daytime, a competition between the warming effect of terrestrial radiation and the cooling effect of solar radiation ensues. The net impact is a decrease in surface temperature, indicating that the effect of solar radiation dominates, with the cooling effect exceeding the warming effect (Sokolik and Toon, 1999).

The regional evaluation in Fig. 5 confirms these contrasting results and indicates a reduction in regional MAE by about 14 % with the coupling rather than with WRF alone. The overestimation of surface temperature in dusty areas with the coupling, not present in the WRF-only simulation, reveals the dominant aerosol warming effect during nighttime compared to the cooling effect during the daytime. These results align with those of Briant et al. (2017), who estimated dust-induced warming of up to +5 °C during nighttime and cooling of approximately −1 °C during the daytime in a 2012 dust event in West Africa. These statements strongly depend on the accuracy of the ERA5 reanalysis which serves as a reference. ERA5 integrates data assimilation of temperature and incorporates aerosol radiative effects through prescribed monthly climatologies from the GO-

CART model but does not dynamically simulate aerosols. Due to the limited ground measurements in the Saharan region to constrain the reanalysis and to the significant biases that can come when considering a coarse climatology for the radiative effects of aerosols to represent an intense dust event, it is possible that ERA5 underestimates the aerosol effect in dusty areas.

Nevertheless, despite the improvements demonstrated in solar irradiance and surface temperature estimation, the WRF–CHIMERE simulations exhibit a notable positive bias in terms of AOD, as evidenced by the local and regional evaluations presented in Figs. 6 and 7. This overestimation cannot be attributed solely to differences in aerosol concentrations, as the simulations yield markedly disparate surface concentrations of PM₁₀, depending on the dust aerosol initial and boundary condition datasets chosen (Fig. 10), while these discrepancies do not appear in the AOD estimates. However, the results from Yahi et al. (2013) and Léon et al. (2020) emphasised the importance of considering dust plume height when linking surface PM₁₀ concentrations to AOD. Therefore, differences in the vertical distribution of the dust plume, which are not evaluated in this study due to the lack of quantitative observational data, could account for part of the observed discrepancies between simulated AODs and surface PM₁₀ concentrations. This excess of aerosol load may be attributed to an overestimation of emissions within the domain, but this cannot be verified as there is no such measurement. The incoming flux of dust in the domain plays a minor role as shown in Fig. 12, where the flux significantly also varies depending on the dust aerosol initial and boundary condition datasets employed, while these differences are no longer present in the simulated AOD estimates. Additionally, the underestimation of aerosol deposition by sedimentation (not studied in this research) could be at the origin of the overestimation of the simulated dust loads. Finally, another potential explanation for these AOD biases may be the inaccuracies in the dust radiative properties incorporated in the CHIMERE model calculation (see Tables S1 and S2). These depend on the mineralogical composition of the desert dust particles emitted, which are considered uniform in this work. The radiative properties of aerosols also depend on their granulometry. In the CHIMERE model, dust aerosols are treated as spherical particles in the calculation of their radiative properties using Mie theory, which introduces biases. Adebisi et al. (2023) showed that ellipsoidal dust particles have a slightly higher mass extinction efficiency compared to spherical particles. As a result, accounting for ellipsoidal dust aerosols would lead to a slight increase in AOD that is associated with a small decrease in GHI. This study further indicates that dust particles with radii smaller than 20.0 μm are the primary contributors to dust AOD for shortwave radiation, with the contribution from larger particles being an order of magnitude lower. Therefore, including particles larger than 40.0 μm in the CHIMERE model would not significantly affect AOD and GHI estimates. This is corrobor-

orated by Mostamandi et al. (2023), who demonstrated that dust particles with radii smaller than $3\ \mu\text{m}$ are primarily responsible for the reduction in solar irradiance, while particles larger than $10\ \mu\text{m}$ mainly contribute to dust deposition, which was not examined in this study.

The uncertainty associated with the choice of the large-scale dust aerosol initial and boundary condition datasets is very low when considering the variables of interest for solar production, namely GHI and surface temperature (Figs. 3 and 5). This uncertainty is also low compared to the performance of simulations for AOD estimation (Fig. 7). This result is similar when examining dust emissions within the domain, which are nearly identical for the three coupled simulations (Fig. 11). This can be explained by the fact that dust emissions depend on the cube of surface wind speed (Marticorena and Bergametti, 1995), which presents no significant signature of the selection of the dust aerosol initial and boundary conditions (Fig. S4). The aerosols emitted within the chosen domain are much greater than those entering, as the domain accounts for the main source zones. This is why the simulations are not that sensitive to dust aerosol large-scale dataset employed. The results regarding the uncertainty associated with the choice of the dust aerosol initial and boundary condition datasets differ when examining various elements of the dust life cycle. Indeed, aerosol size distributions vary significantly between the simulation driven with GOCART on the one hand and simulations driven with CAMS and MERRA-2 on the other hand. GOCART climatology over-represents aerosols larger than $10\ \mu\text{m}$ compared to the CAMS and MERRA-2 reanalyses. These differences partially account for the significant deviation in surface PM_{10} concentration estimates (Fig. 10), indicating that reanalysis-type datasets result in much higher values, up to 3 times higher, compared to climatological-type data, which are closer to ground observations. The dust flux entering the domain may also partly explain these differences. In fact, this flux is very low with GOCART, with values up to 3.5 times lower than CAMS and MERRA-2 (Fig. 12). The size distribution of this incoming aerosol flux is also a determining factor.

4 Conclusion and perspectives

This study aims to evaluate the ability of the WRF–CHIMERE coupling to simulate GHI during a typical dust event in the dry season in West Africa. This event is characterised by a Harmattan flux associated with significant desert dust emissions over the Bodélé Depression, with the dust plume subsequently transported westward. This work demonstrates the utility of coupling a meteorological model with a desert aerosol life cycle model to represent such events, particularly for improving solar forecasts. Indeed, GHI estimations are markedly enhanced with this approach compared to using a meteorological model alone with a

75 % reduction in the local MAE. Nevertheless, the performance of the WRF–CHIMERE simulations in representing the aerosol load of this event is more controversial. There is an overall overestimation of AOD and PM_{10} surface concentration by the coupled model in the north Sahelian–Saharan zone.

This work also aims at investigating whether the performance of the simulations can be improved by changing the dust aerosol initial and boundary condition datasets and at estimating the uncertainty associated with this choice. The results show that this selection has almost no influence on the estimation of the solar irradiance, surface temperature, and AOD. On the contrary, the choice of the dust aerosol initial and boundary condition datasets has a significant impact on the surface PM_{10} concentration and the aerosol size distribution.

This work outlines new research perspectives. First, we observe the difficulty of evaluating simulations in West Africa due to the scarcity of available observations. Establishing a denser measurement network or conducting observation campaigns, particularly for GHI, would help research about the solar estimation and forecasting in this region. Additionally, the WRF–CHIMERE simulations demonstrate significant biases in terms of AOD and PM_{10} surface concentration which are not fully explained here. One potential explanation for this is an overestimation of dust emission for which no evaluation is possible. Furthermore, studying aerosol deposition (not conducted in this work) would complement the study of the desert dust aerosol life cycle. On the one hand, an underestimation of the deposition might be a contributing factor to the overestimation of the simulated aerosol load. On the other hand, dust deposition on solar panels affects solar production by masking the available solar irradiance (soiling effect), and this should be taken into account in forecasting systems to conduct optimised cleaning operations. A further limitation of this study is the use of the WRF meteorological model for the coupling with CHIMERE rather than the WRF–Solar model (Jimenez et al., 2016), which is an enhanced version of WRF dedicated to solar forecasting. Indeed, WRF–Solar incorporates enhanced algorithms for the computation of solar irradiance, accounting for the direct and indirect effects of aerosols and employing an advanced solar-tracking algorithm. This makes it the appropriate version of WRF to use for solar energy research. However, no coupling between WRF–Solar and CHIMERE has yet been implemented, representing an important perspective to expand this work. Finally, the study focuses on a typical dust event during the dry season, essentially presenting the aerosol–radiation interaction. It could be beneficial to test such a simulation configuration for more complex cases involving cloud presence. Indeed, the interaction between aerosols and clouds has a significant impact on solar forecasting by increasing albedo, extending cloud lifespan, and promoting cloud formation through increased condensation nucleus concentration (indirect aerosol effects).

Code and data availability. WRF namelist configuration files, CHIMERE parameter files, Python codes exploited in this study, and GOCART climatology data can be found in the Zenodo repository at <https://doi.org/10.5281/zenodo.10808476> (Clauzel, 2024).

ERA5 data are available from the Copernicus Climate Data Store service at <https://doi.org/10.24381/cds.adbb2d47> (Hersbach et al., 2023).

CAMS data were downloaded from the Copernicus Atmosphere Data Store service at <https://ads.atmosphere.copernicus.eu/datasets?q=CAMS> (Qu et al., 2017; Inness et al., 2019; Schroedter-Homscheidt, et al., 2022).

MERRA-2 data can be found on the dedicated NASA platform at <https://goldsmr5.gesdisc.eosdis.nasa.gov/data/MERRA2/> (Gelaro et al., 2017).

Data from AMMA ground measurement stations can be accessed from <https://doi.org/10.17178/AMMA-CATCH.all> (AMMA-CATCH, 1990).

The INDAAF web page allows access to the data at <https://indaaf.obs-mip.fr/catalogue/> (last access: 2 September 2024; <https://doi.org/10.25326/210>, Rajot et al., 2010a; <https://doi.org/10.25326/269>, Rajot et al., 2010b; <https://doi.org/10.25326/268>, Rajot et al., 2010c; <https://doi.org/10.25326/263>, Marticorena et al., 2021a; <https://doi.org/10.25326/267>, Marticorena et al., 2021b; Kaly et al., 2015).

AOD and aerosol inversion data are available from the AERONET website (<https://aeronet.gsfc.nasa.gov>, AERONET, 2024), and the website provides these data freely to the public. Data may be acquired by utilizing several download mechanisms including site-by-site download tools.

The MODIS satellite observations are available from NASA's Level-1 and Atmosphere Archive and Distribution System Distributed Active Archive Center (LAADS DAAC) platform at https://doi.org/10.5067/MODIS/MOD08_D3.061 (Platnick et al., 2015).

Supplement. The supplement related to this article is available online at: <https://doi.org/10.5194/acp-25-997-2025-supplement>.

Author contributions. LC, SA, and CL conceptualised the study. LC performed the simulations, the analysis, and the compilations of the figures. LC, SA, CL, GB, BM, GS, CB, RL, and JT discussed the results. LC wrote the paper.

Competing interests. The contact author has declared that none of the authors has any competing interests.

Disclaimer. Publisher's note: Copernicus Publications remains neutral with regard to jurisdictional claims made in the text, published maps, institutional affiliations, or any other geographical representation in this paper. While Copernicus Publications makes every effort to include appropriate place names, the final responsibility lies with the authors.

Acknowledgements. To conduct the simulations, this study has benefited from access to the IPSL-SU (SPIRIT) cluster within the ESPRI IPSL mesocentre facility supported by CNRS, UPMC, Labex L-IPSL, CNES, and École Polytechnique. The authors thank the WRF and CHIMERE developers for giving free access to their model. We thank the National Aeronautics and Space Agency for the availability of the MODIS and the MERRA-2 data; the European Centre for Medium-Range Weather Forecasts for the availability of the CAMS and ERA5 data; and the investigators and staff, who maintain and provide the AERONET, INDAAF, and AMMA-CATCH observational data. Finally, we thank the company Sonabel for their contribution.

During the preparation of this work, the authors used DeepL Write (DeepL SE) in order to improve language and readability. After using this tool/service, the authors reviewed and edited the content as needed and take full responsibility for the content of the publication.

Financial support. This research has been supported by the NETWAT project operated by the French National Research Agency (grant no. ANR-22-CE03-0011).

Review statement. This paper was edited by Marco Gaetani and reviewed by two anonymous referees.

References

- Adebiyi, A., Kok, J. F., Murray, B. J., Ryder, C. L., Stuu, J.-B. W., Kahn, R. A., Knippertz, P., Formenti, P., Mahowald, N. M., Pérez García-Pando, C., Klose, M., Ansmann, A., Samset, B. H., Ito, A., Balkanski, Y., Di Biagio, C., Romanias, M. N., Huang, Y., and Meng, J.: A review of coarse mineral dust in the Earth system, *Aeolian Res.*, 60, 100849, <https://doi.org/10.1016/j.aeolia.2022.100849>, 2023.
- AERONET: AOD and aerosol inversion data, AEROSOL ROBOTIC NETWORK, NASA, <https://aeronet.gsfc.nasa.gov>, last access: 2 September 2024.
- Aidara, M. C., Fam, P. A., Danso, D. K., Mortey, E. M., Mbaye, A., Ndiaye, M. L., Bonkaney, A. L., Adamou, R., Anquetin, S., and Diedhiou, A.: Contribution to the building of a weather information service for solar panel cleaning operations at Diass plant (Senegal, Western Sahel), *Open Geosci.*, 15, 20220449, <https://doi.org/10.1515/geo-2022-0449>, 2023.
- Alfaro, S. C. and Gomes, L.: Modeling mineral aerosol production by wind erosion: Emission intensities and aerosol size distributions in source areas, *J. Geophys. Res.-Atmos.*, 106, 18075–18084, <https://doi.org/10.1029/2000JD900339>, 2001.
- AMMA-CATCH: AMMA-CATCH: a hydrological, meteorological and ecological observatory on West Africa, IRD, CNRS-INSU, OSUG, OMP, OREME [data set], <https://doi.org/10.17178/AMMA-CATCH.all>, 1990.
- Arakawa, A.: The Cumulus Parameterization Problem: Past, Present, and Future, *J. Climate*, 17, 2493–2525, [https://doi.org/10.1175/1520-0442\(2004\)017<2493:RATCPP>2.0.CO;2](https://doi.org/10.1175/1520-0442(2004)017<2493:RATCPP>2.0.CO;2), 2004.

- Bergametti, G., Marticorena, B., Rajot, J. L., Chatenet, B., Féron, A., Gaimoz, C., Siour, G., Coulibaly, M., Koné, I., Maman, A., and Zakou, A.: Dust Uplift Potential in the Central Sahel: An Analysis Based on 10 years of Meteorological Measurements at High Temporal Resolution, *J. Geophys. Res.-Atmos.*, 122, 12433–12448, <https://doi.org/10.1002/2017JD027471>, 2017.
- Bian, H. and Prather, M. J.: Fast-J2: Accurate Simulation of Stratospheric Photolysis in Global Chemical Models, *J. Atmos. Chem.*, 41, 281–296, <https://doi.org/10.1023/A:1014980619462>, 2002.
- Bou Karam, D., Flamant, C., Tulet, P., Chaboureau, J.-P., Dabas, A., and Todd, M. C.: Estimate of Sahelian dust emissions in the intertropical discontinuity region of the West African Monsoon, *J. Geophys. Res.-Atmos.*, 114, D13106, <https://doi.org/10.1029/2008JD011444>, 2009.
- Briant, R., Tuccella, P., Deroubaix, A., Khvorostyanov, D., Menut, L., Mailler, S., and Turquety, S.: Aerosol–radiation interaction modelling using online coupling between the WRF 3.7.1 meteorological model and the CHIMERE 2016 chemistry-transport model, through the OASIS3-MCT coupler, *Geosci. Model Dev.*, 10, 927–944, <https://doi.org/10.5194/gmd-10-927-2017>, 2017.
- Clauzel, L.: Solar radiation estimation in West Africa: impact of dust conditions during 2021 dry season, Zenodo [data set], <https://doi.org/10.5281/zenodo.10808476>, 2024.
- Clauzel, L., Anquetin, S., Lavaysse, C., Tremoy, G., and Raynaud, D.: West African operational daily solar forecast errors and their link with meteorological conditions, *Renew. Energy*, 224, 120101, <https://doi.org/10.1016/j.renene.2024.120101>, 2024.
- Dajuma, A., Yahaya, S., Touré, S., Diedhiou, A., Adamou, R., Konaré, A., Sido, M., and Golba, M.: Sensitivity of Solar Photovoltaic Panel Efficiency to Weather and Dust over West Africa: Comparative Experimental Study between Niamey (Niger) and Abidjan (Côte d’Ivoire), *Computational Water, Energy, and Environmental Engineering*, 5, 123–147, <https://doi.org/10.4236/cweee.2016.54012>, 2016.
- D’Almeida, G. A.: A Model for Saharan Dust Transport, *J. Appl. Meteorol. Clim.*, 25, 903–916, [https://doi.org/10.1175/1520-0450\(1986\)025<0903:AMFSDT>2.0.CO;2](https://doi.org/10.1175/1520-0450(1986)025<0903:AMFSDT>2.0.CO;2), 1986.
- Diabaté, L., Blanc, P., and Wald, L.: Solar radiation climate in Africa, *Sol. Energy*, 76, 733–744, 2004.
- Diop, D., Drame, M. S., Diallo, M., Malec, D., Mary, D., and Guillot, P.: Modelling of Photovoltaic Modules Optical Losses Due to Saharan Dust Deposition in Dakar, Senegal, West Africa, *Smart Grid and Renewable Energy*, 11, 89–102, <https://doi.org/10.4236/sgre.2020.117007>, 2020.
- Dubovik, O. and King, M. D.: A flexible inversion algorithm for retrieval of aerosol optical properties from Sun and sky radiance measurements, *J. Geophys. Res.-Atmos.*, 105, 20673–20696, <https://doi.org/10.1029/2000JD900282>, 2000.
- El Alani, O., Ghennioui, A., Ghennioui, H., Saint-Drenan, Y.-M., and Blanc, P.: Evaluation of 24-Hours forecasts of global solar irradiation from IFS, GFS and McClear models, *AIP Conf. Proc.*, 2307, 020053, <https://doi.org/10.1063/5.0032744>, 2020.
- Engelstaedter, S. and Washington, R.: Atmospheric controls on the annual cycle of North African dust, *J. Geophys. Res.-Atmos.*, 112, D03103, <https://doi.org/10.1029/2006JD007195>, 2007.
- Engelstaedter, S., Tegen, I., and Washington, R.: North African dust emissions and transport, *Earth-Sci. Rev.*, 79, 73–100, <https://doi.org/10.1016/j.earscirev.2006.06.004>, 2006.
- Evans, M., Knippertz, P., Akpo, A., Allan, R. P., Amekudzi, L., Brooks, B., Chiu, J. C., Coe, H., Fink, A. H., Flamant, C., Jegede, O. O., Leal-Liousse, C., Lohou, F., Kalthoff, N., Mari, C., Marsham, J. H., Yoboué, V., and Zumsprekel, C. R.: Policy findings from the DACCIWA Project, Zenodo [report], <https://doi.org/10.5281/zenodo.1476843>, 2018.
- Fécán, F., Marticorena, B., and Bergametti, G.: Parametrization of the increase of the aeolian erosion threshold wind friction velocity due to soil moisture for arid and semi-arid areas, *Ann. Geophys.*, 17, 149–157, <https://doi.org/10.1007/s00585-999-0149-7>, 1999.
- Flamant, C., Chaboureau, J.-P., Delanoë, J., Gaetani, M., Jamet, C., Lavaysse, C., Bock, O., Borne, M., Cazenave, Q., Coutris, P., Cuesta, J., Menut, L., Aubry, C., Benedetti, A., Bosser, P., Bounissou, S., Caudoux, C., Collomb, H., Donal, T., Febvre, G., Fehr, T., Fink, A. H., Formenti, P., Araujo, N. G., Knippertz, P., Lecuyer, E., Andrade, M. N., Langué, C. G. N., Jonville, T., Schwarzenboeck, A., and Takeishi, A.: Cyclogenesis in the Tropical Atlantic: First Scientific Highlights from the Clouds–Atmospheric Dynamics–Dust Interactions in West Africa (CAD-DIWA) Field Campaign, *B. Am. Meteorol. Soc.*, 105, E387–E417, <https://doi.org/10.1175/BAMS-D-23-0230.1>, 2024.
- Galle, S., Grippa, M., Peugeot, C., Moussa, I.B., Cappelaere, B., Demarty, J., Mougou, E., Panthou, G., Adjomayi, P., Agbossou, E. K., Ba, A., Boucher, M., Cohard, J., Descloitres, M., Descroix, L., Diawara, M., Dossou, M., Favreau, G., Gangneron, F., Gosset, M., Hector, B., Hiernaux, P., Issoufou, B., Kergoat, L., Lawin, E., Lebel, T., Legchenko, A., Abdou, M. M., Malam-Issa, O., Mamadou, O., Nazoumou, Y., Pellarin, T., Quantin, G., Sambou, B., Seghieri, J., Séguis, L., Vandervaere, J., Vischel, T., Vouillamoz, J., Zannou, A., Afouda, S., Alhassane, A., Arjounin, M., Baral, H., Biron, R., Cazenave, F., Chaffard, V., Chazarin, J., Guyard, H., Koné, A., Mainassara, I., Mamane, A., Oi, M., Ouani, T., Soumaguel, N., Wubda, M., Ago, E. E., Alle, I. C., Allies, A., Arpin-Pont, F., Awessou, B., Cassé, C., Charvet, G., Dardel, C., Depeyre, A., Diallo, F. B., Do, T., Fatras, C., Frappart, F., Gal, L., Gascon, T., Gibon, F., Guiro, I., Ingatan, A., Kempf, J., Kotchoni, D. O. V., Lawson, F. M. A., Leauthaud, C., Louvet, S., Mason, E., Nguyen, C. C., Perrimond, B., Pierre, C., Richard, A., Robert, E., Román-Cascón, C., Velluet, C., and Wilcox, C.: AMMA-CATCH, a Critical Zone Observatory in West Africa Monitoring a Region in Transition, *Vadose Zone J.*, 17, 1–24, <https://doi.org/10.2136/vzj2018.03.0062>, 2018.
- Gelaro, R., McCarty, W., Suárez, M. J., Todling, R., Molod, A., Takacs, L., Randles, C. A., Darmenov, A., Bosilovich, M. G., Reichle, R., Wargan, K., Coy, L., Cullather, R., Draper, C., Akella, S., Buchard, V., Conaty, A., Silva, A. M. da, Gu, W., Kim, G.-K., Koster, R., Lucchesi, R., Merkova, D., Nielsen, J. E., Parityka, G., Pawson, S., Putman, W., Rienecker, M., Schubert, S. D., Sienkiewicz, M., and Zhao, B.: The Modern-Era Retrospective Analysis for Research and Applications, Version 2 (MERRA-2), *J. Climate*, 30, 5419–5454, <https://doi.org/10.1175/JCLI-D-16-0758.1>, 2017 (data available at: <https://goldsmr5.gesdisc.eosdis.nasa.gov/data/MERRA2/>, last access: 2 September 2024).
- Giles, D. M., Sinyuk, A., Sorokin, M. G., Schafer, J. S., Smirnov, A., Slutsker, I., Eck, T. F., Holben, B. N., Lewis, J. R., Campbell, J. R., Welton, E. J., Korkin, S. V., and Lyapustin, A. I.: Advancements in the Aerosol Robotic Network (AERONET) Version 3 database – automated near-real-time quality control algorithm

- with improved cloud screening for Sun photometer aerosol optical depth (AOD) measurements, *Atmos. Meas. Tech.*, 12, 169–209, <https://doi.org/10.5194/amt-12-169-2019>, 2019.
- Ginoux, P., Chin, M., Tegen, I., Prospero, J. M., Holben, B., Dubovik, O., and Lin, S.-J.: Sources and distributions of dust aerosols simulated with the GOCART model, *J. Geophys. Res.-Atmos.*, 106, 20255–20273, <https://doi.org/10.1029/2000JD000053>, 2001.
- Hauglustaine, D. A., Hourdin, F., Jourdain, L., Filiberti, M.-A., Walters, S., Lamarque, J.-F., and Holland, E. A.: Interactive chemistry in the Laboratoire de Météorologie Dynamique general circulation model: Description and background tropospheric chemistry evaluation, *J. Geophys. Res.-Atmos.*, 109, D04314, <https://doi.org/10.1029/2003JD003957>, 2004.
- Hersbach, H., Bell, B., Berrisford, P., Hirahara, S., Horányi, A., Muñoz-Sabater, J., Nicolas, J., Peubey, C., Radu, R., Schepers, D., Simmons, A., Soci, C., Abdalla, S., Abellan, X., Balsamo, G., Bechtold, P., Biavati, G., Bidlot, J., Bonavita, M., De Chiara, G., Dahlgren, P., Dee, D., Diamantakis, M., Dragani, R., Flemming, J., Forbes, R., Fuentes, M., Geer, A., Haimberger, L., Healy, S., Hogan, R. J., Hólm, E., Janisková, M., Keeley, S., Laloyaux, P., Lopez, P., Lupu, C., Radnoti, G., de Rosnay, P., Rozum, I., Vamborg, F., Villaume, S., and Thépaut, J.-N.: The ERA5 global reanalysis, *Q. J. Roy. Meteorol. Soc.*, 146, 1999–2049, <https://doi.org/10.1002/qj.3803>, 2020.
- Hersbach, H., Bell, B., Berrisford, P., Biavati, G., Horányi, A., Muñoz Sabater, J., Nicolas, J., Peubey, C., Radu, R., Rozum, I., Schepers, D., Simmons, A., Soci, C., Dee, D., and Thépaut, J.-N.: ERA5 hourly data on single levels from 1940 to present, Copernicus Climate Change Service (C3S) Climate Data Store (CDS) [data set], <https://doi.org/10.24381/cds.adbb2d47>, 2023.
- Holben, B. N., Eck, T. F., Slutsker, I., Tanré, D., Buis, J. P., Setzer, A., Vermote, E., Reagan, J. A., Kaufman, Y. J., Nakajima, T., Lavenu, F., Jankowiak, I., and Smirnov, A.: AERONET – A Federated Instrument Network and Data Archive for Aerosol Characterization, *Remote Sens. Environ.*, 66, 1–16, [https://doi.org/10.1016/S0034-4257\(98\)00031-5](https://doi.org/10.1016/S0034-4257(98)00031-5), 1998.
- Hu, X.-M., Klein, P. M., and Xue, M.: Evaluation of the updated YSU planetary boundary layer scheme within WRF for wind resource and air quality assessments, *J. Geophys. Res.-Atmos.*, 118, 10490–10505, <https://doi.org/10.1002/jgrd.50823>, 2013.
- Iacono, M. J., Delamere, J. S., Mlawer, E. J., Shephard, M. W., Clough, S. A., and Collins, W. D.: Radiative forcing by long-lived greenhouse gases: Calculations with the AER radiative transfer models, *J. Geophys. Res.-Atmos.*, 113, D13103, <https://doi.org/10.1029/2008JD009944>, 2008.
- IEA: Africa Energy Outlook 2022, IEA, Paris, <https://www.iea.org/reports/africa-energy-outlook-2022> (last access: 2 September 2024), 2022.
- Inness, A., Ades, M., Agustí-Panareda, A., Barré, J., Benedictow, A., Blechschmidt, A.-M., Dominguez, J. J., Engelen, R., Eskes, H., Flemming, J., Huijnen, V., Jones, L., Kipling, Z., Massart, S., Parrington, M., Peuch, V.-H., Razinger, M., Remy, S., Schulz, M., and Suttie, M.: The CAMS reanalysis of atmospheric composition, *Atmos. Chem. Phys.*, 19, 3515–3556, <https://doi.org/10.5194/acp-19-3515-2019>, 2019.
- Jiménez, P. A., Dudhia, J., González-Rouco, J. F., Navarro, J., Montávez, J. P., and García-Bustamante, E.: A Revised Scheme for the WRF Surface Layer Formulation, *Mon. Weather Rev.*, 140, 898–918, <https://doi.org/10.1175/MWR-D-11-00056.1>, 2012.
- Jimenez, P. A., Hacker, J. P., Dudhia, J., Haupt, S. E., Ruiz-Arias, J. A., Gueymard, C. A., Thompson, G., Eidhammer, T., and Deng, A.: WRF-Solar: Description and Clear-Sky Assessment of an Augmented NWP Model for Solar Power Prediction, *B. Am. Meteorol. Soc.*, 97, 1249–1264, <https://doi.org/10.1175/BAMS-D-14-00279.1>, 2016.
- Kaly, F., Marticorena, B., Chatenet, B., Rajot, J. L., Janicot, S., Niang, A., Yahi, H., Thiria, S., Maman, A., Zakou, A., Coulibaly, B. S., Coulibaly, M., Koné, I., Traoré, S., Diallo, A., and Ndiaye, T.: Variability of mineral dust concentrations over West Africa monitored by the Sahelian Dust Transect, *Atmos. Res.*, 164–165, 226–241, <https://doi.org/10.1016/j.atmosres.2015.05.011>, 2015.
- Klose, M., Shao, Y., Karremann, M. K., and Fink, A. H.: Sahel dust zone and synoptic background, *Geophys. Res. Lett.*, 37, L09802, <https://doi.org/10.1029/2010GL042816>, 2010.
- Klüser, L., Killius, N., and Gesell, G.: APOLLO_NG – a probabilistic interpretation of the APOLLO legacy for AVHRR heritage channels, *Atmos. Meas. Tech.*, 8, 4155–4170, <https://doi.org/10.5194/amt-8-4155-2015>, 2015.
- Kok, J. F., Adebisi, A. A., Albani, S., Balkanski, Y., Checa-Garcia, R., Chin, M., Colarco, P. R., Hamilton, D. S., Huang, Y., Ito, A., Klose, M., Li, L., Mahowald, N. M., Miller, R. L., Obiso, V., Pérez García-Pando, C., Rocha-Lima, A., and Wan, J. S.: Contribution of the world’s main dust source regions to the global cycle of desert dust, *Atmos. Chem. Phys.*, 21, 8169–8193, <https://doi.org/10.5194/acp-21-8169-2021>, 2021.
- Lefèvre, M.: CAMS solar radiation evaluation and quality assurance report #34, March–May 2021, ECMWF COPERNICUS REPORT, https://atmosphere.copernicus.eu/sites/default/files/custom-uploads/EQC-solar/CAMS2_73_2021SC1_D1.3.1-2021Q4_RAD_validation_report_MAM2021_v1.pdf (last access: 10 September 2024), 2022.
- Léon, J.-F., Martiny, N., and Merlet, S.: A Multi Linear Regression Model to Derive Dust PM₁₀ in the Sahel Using AERONET Aerosol Optical Depth and CALIOP Aerosol Layer Products, *Remote Sens.*, 12, 3099, <https://doi.org/10.3390/rs12183099>, 2020.
- Marshall, J. H., Parker, D. J., Grams, C. M., Johnson, B. T., Grey, W. M. F., and Ross, A. N.: Observations of mesoscale and boundary-layer scale circulations affecting dust transport and uplift over the Sahara, *Atmos. Chem. Phys.*, 8, 6979–6993, <https://doi.org/10.5194/acp-8-6979-2008>, 2008.
- Marticorena, B. and Bergametti, G.: Modeling the atmospheric dust cycle: 1. Design of a soil-derived dust emission scheme, *J. Geophys. Res.-Atmos.*, 100, 16415–16430, <https://doi.org/10.1029/95JD00690>, 1995.
- Marticorena, B., Chatenet, B., Rajot, J. L., Traoré, S., Coulibaly, M., Diallo, A., Koné, I., Maman, A., NDiaye, T., and Zakou, A.: Temporal variability of mineral dust concentrations over West Africa: analyses of a pluriannual monitoring from the AMMA Sahelian Dust Transect, *Atmos. Chem. Phys.*, 10, 8899–8915, <https://doi.org/10.5194/acp-10-8899-2010>, 2010.
- Marticorena, B., Dorego, G. S., Rajot, J. L., Bouet, C., Allègre, M., Chatenet, B., Féron, A., Gaimoz, C., Siour, G., Valorso, R., Diop, M., Der Ba, S., Rokhy N’Diaye, G., Séné, M., and Thiam, A.: Air temperature, Bambey, Senegal, Aeris [data set], <https://doi.org/10.25326/263>, 2021a.

- Marticorena, B., Dorego, G. S., Rajot, J. L., Bouet, C., Allègre, M., Chatenet, B., Féron, A., Gaimoz, C., Maisonneuve, F., Siour, G., Valorso, R., Diop, M., Der Ba, S., Rokhy N'Diaye, G., Séné, M., and Thiam, A.: PM₁₀ concentration, Bambey, Senegal, AERIS [data set], <https://doi.org/10.25326/267>, 2021b.
- Masoom, A., Kosmopoulos, P., Bansal, A., Gkikas, A., Proestakis, E., Kazadzis, S., and Amiridis, V.: Forecasting dust impact on solar energy using remote sensing and modeling techniques, *Sol. Energy*, 228, 317–332, <https://doi.org/10.1016/j.solener.2021.09.033>, 2021.
- Menut, L.: Variability and combination as an ensemble of mineral dust forecasts during the 2021 CADDIWA experiment using the WRF 3.7.1 and CHIMERE v2020r3 models, *Geosci. Model Dev.*, 16, 4265–4281, <https://doi.org/10.5194/gmd-16-4265-2023>, 2023.
- Menut, L., Siour, G., Mailler, S., Couvidat, F., and Bessagnet, B.: Observations and regional modeling of aerosol optical properties, speciation and size distribution over Northern Africa and western Europe, *Atmos. Chem. Phys.*, 16, 12961–12982, <https://doi.org/10.5194/acp-16-12961-2016>, 2016.
- Menut, L., Bessagnet, B., Briant, R., Cholakian, A., Couvidat, F., Mailler, S., Pennel, R., Siour, G., Tuccella, P., Turquety, S., and Valari, M.: The CHIMERE v2020r1 online chemistry-transport model, *Geosci. Model Dev.*, 14, 6781–6811, <https://doi.org/10.5194/gmd-14-6781-2021>, 2021.
- Mostamandi, S., Ukhov, A., Engelbrecht, J., Shevchenko, I., Osipov, S., and Stenchikov, G.: Fine and Coarse Dust Effects on Radiative Forcing, Mass Deposition, and Solar Devices Over the Middle East, *J. Geophys. Res.-Atmos.*, 128, e2023JD039479, <https://doi.org/10.1029/2023JD039479>, 2023.
- Mueller, R., Pfeifroth, U., and Traeger-Chatterjee, C.: Towards Optimal Aerosol Information for the Retrieval of Solar Surface Radiation Using Heliosat, *Atmosphere*, 6, 863–878, <https://doi.org/10.3390/atmos6070863>, 2015.
- Niu, G.-Y., Yang, Z.-L., Mitchell, K. E., Chen, F., Ek, M. B., Barlage, M., Kumar, A., Manning, K., Niyogi, D., Rosero, E., Tewari, M., and Xia, Y.: The community Noah land surface model with multiparameterization options (Noah-MP): 1. Model description and evaluation with local-scale measurements, *J. Geophys. Res.-Atmos.*, 116, D12109, <https://doi.org/10.1029/2010JD015139>, 2011.
- Ochiegbu, D. C.: Event of harmattan dust transport in Kano State of Nigeria, *International Journal of Scientific and Research Publications*, 11, 205–210, <https://doi.org/10.29322/IJSRP.11.08.2021.p11628>, 2021.
- Plain, N., Hingray, B., and Mathy, S.: Accounting for low solar resource days to size 100 % solar microgrids power systems in Africa, *Renew. Energ.*, 131, 448–458, <https://doi.org/10.1016/j.renene.2018.07.036>, 2018.
- Platnick, S., et al.: MODIS Atmosphere L3 Daily Product, NASA MODIS Adaptive Processing System, Goddard Space Flight Center, USA [data set], https://doi.org/10.5067/MODIS/MOD08_D3.061, 2015.
- Prigent, C., Jiménez, C., and Catherinot, J.: Comparison of satellite microwave backscattering (ASCAT) and visible/near-infrared reflectances (PARASOL) for the estimation of aeolian aerodynamic roughness length in arid and semi-arid regions, *Atmos. Meas. Tech.*, 5, 2703–2712, <https://doi.org/10.5194/amt-5-2703-2012>, 2012.
- Prospero, J. M., Ginoux, P., Torres, O., Nicholson, S. E., and Gill, T. E.: Environmental Characterization of Global Sources of Atmospheric Soil Dust Identified with the Nimbus 7 Total Ozone Mapping Spectrometer (toms) Absorbing Aerosol Product, *Rev. Geophys.*, 40, 1002, <https://doi.org/10.1029/2000RG000095>, 2002.
- Qu, Z., Oumbe, A., Blanc, P., Espinar, B., Gesell, G., Gschwind, B., Klüser, L., Lefèvre, M., Saboret, L., Schroedter-Homscheidt, M., and Wald, L.: Fast radiative transfer parameterisation for assessing the surface solar irradiance: The Heliosat-4 method, *Meteorol. Z.*, 26, 33–57, <https://doi.org/10.1127/metz/2016/0781>, 2017 (data available at: <https://ads.atmosphere.copernicus.eu/datasets?q=CAMS>, last access: 2 September 2024).
- Rajot, J. L., Abdourhamane Touré, A., Marticorena, B., Bouet, C., Allègre, M., Chatenet, B., Féron, A., Gaimoz, C., Siour, G., Valorso, R., Maman, A., and Zakou, A.: Air temperature, Banizoumbou, Niger, AERIS [data set], <https://doi.org/10.25326/210>, 2010a.
- Rajot, J. L., Boubacar, A., Marticorena, B., Bouet, C., Allègre, M., Chatenet, B., Féron, A., Gaimoz, C., Siour, G., Valorso, R., Coulibaly, S. B., Kouyaté, Z., Coulibaly, B., Coulibaly, M., Koné, I., and Traoré, S.: Air temperature, Cinzana, Mali, AERIS [data set], <https://doi.org/10.25326/269>, 2010b.
- Rajot, J. L., Boubacar, A., Marticorena, B., Bouet, C., Allègre, M., Chatenet, B., Féron, A., Gaimoz, C., Maisonneuve, F., Siour, G., Valorso, R., Coulibaly, S. B., Kouyaté, Z., Coulibaly, B., Coulibaly, M., Koné, I., and Traoré, S.: PM₁₀ concentration, Cinzana, Mali, AERIS [data set], <https://doi.org/10.25326/268>, 2010c.
- Redelsperger, J.-L., Diedhiou, A., Flamant, C., Janicot, S., Lafore, J.-P., Lebel, T., Polcher, J., Bourlès, B., Caniaux, G., Rosnay, P. de, Desbois, M., Eymard, L., Fontaine, B., Geneau, I., Ginoux, K., Hoepffner, M., Kane, C. S. E., Law, K. S., Mari, C., Marticorena, B., Mougin, É., Pelon, J., Peugeot, C., Protat, A., Roux, F., Sultan, B., and Akker, E. van den: Amma, une étude multidisciplinaire de la mousson ouest-africaine, *La Météorologie*, 54, 22–32, <https://doi.org/10.4267/2042/20098>, 2006.
- Sawadogo, W., Bliefernicht, J., Fersch, B., Salack, S., Guug, S., Diallo, B., Ogunjobi, K. O., Nakoulma, G., Tanu, M., Meilinger, S., and Kunstmann, H.: Hourly global horizontal irradiance over West Africa: A case study of one-year satellite- and reanalysis-derived estimates vs. in situ measurements, *Renew. Energ.*, 216, 119066, <https://doi.org/10.1016/j.renene.2023.119066>, 2023.
- Sawadogo, W., Fersch, B., Bliefernicht, J., Meilinger, S., Rummler, T., Salack, S., Guug, S., and Kunstmann, H.: Evaluation of the WRF-solar model for 72-hour ahead forecasts of global horizontal irradiance in West Africa: A case study for Ghana, *Sol. Energy*, 271, 112413, <https://doi.org/10.1016/j.solener.2024.112413>, 2024.
- Schepanski, K., Tegen, I., Todd, M. C., Heinold, B., Bönisch, G., Laurent, B., and Macke, A.: Meteorological processes forcing Saharan dust emission inferred from MSG-SEVIRI observations of subdaily dust source activation and numerical models, *J. Geophys. Res.-Atmos.*, 114, D10201, <https://doi.org/10.1029/2008JD010325>, 2009.
- Schroedter-Homscheidt, M., Azam, F., Betcke, J., Hanrieder, N., Lefevre, M., Saboret, L., and Saint-Drenan, Y.-M.: Surface solar irradiation retrieval from MSG/SEVIRI based on APOLLO Next Generation and HELIOSAT-4 methods, *Meteorol. Z.*, 31, 455–476, 2022.

- Shao, Y. and Lu, H.: A simple expression for wind erosion threshold friction velocity, *J. Geophys. Res.-Atmos.*, 105, 22437–22443, <https://doi.org/10.1029/2000JD900304>, 2000.
- Skamarock, W., Klemp, J., Dudhia, J., Gill, D. O., Barker, D., Duda, M. G., Huang, X.-Y., Wang, W., and Powers, J. G.: A Description of the Advanced Research WRF Version 3, University Corporation for Atmospheric Research, <https://doi.org/10.5065/D68S4MVH>, 2008.
- Sokolik, I. and Toon, O. B.: Incorporation of mineralogical composition into models of the radiative properties of mineral aerosol from UV to IR wavelengths, *J. Geophys. Res.*, 104, 9423–9444, <https://doi.org/10.1029/1998JD200048>, 1999.
- Thompson, G. and Eidhammer, T.: A Study of Aerosol Impacts on Clouds and Precipitation Development in a Large Winter Cyclone, *J. Atmos. Sci.*, 71, 3636–3658, <https://doi.org/10.1175/JAS-D-13-0305.1>, 2014.
- Tuccella, P., Menut, L., Briant, R., Deroubaix, A., Khvorostyanov, D., Mailler, S., Siour, G., and Turquety, S.: Implementation of Aerosol-Cloud Interaction within WRF-CHIMERE Online Coupled Model: Evaluation and Investigation of the Indirect Radiative Effect from Anthropogenic Emission Reduction on the Benelux Union, *Atmosphere*, 10, 20, <https://doi.org/10.3390/atmos10010020>, 2019.
- UNFCCC: The Paris Agreement, United Nations Framework Convention on Climate Change, <https://unfccc.int/process-and-meetings/the-paris-agreement> (last access: 12 February 2024), 2015.
- Vautard, R., Bessagnet, B., Chin, M., and Menut, L.: On the contribution of natural Aeolian sources to particulate matter concentrations in Europe: Testing hypotheses with a modelling approach, *Atmos. Environ.*, 39, 3291–3303, <https://doi.org/10.1016/j.atmosenv.2005.01.051>, 2005.
- Washington, R. and Todd, M. C.: Atmospheric controls on mineral dust emission from the Bodélé Depression, Chad: The role of the low level jet, *Geophys. Res. Lett.*, 32, L17701, <https://doi.org/10.1029/2005GL023597>, 2005.
- Washington, R., Todd, M. C., Engelstaedter, S., Mbainayel, S., and Mitchell, F.: Dust and the low-level circulation over the Bodélé Depression, Chad: Observations from BoDEX 2005, *J. Geophys. Res.-Atmos.*, 111, D03201, <https://doi.org/10.1029/2005JD006502>, 2006.
- Wild, O., Zhu, X., and Prather, M. J.: Fast-J: Accurate Simulation of In- and Below-Cloud Photolysis in Tropospheric Chemical Models, *J. Atmos. Chem.*, 37, 245–282, <https://doi.org/10.1023/A:1006415919030>, 2000.
- Willis, P. T. and Tattelman, P.: Drop-Size Distributions Associated with Intense Rainfall, *J. Appl. Meteorol.*, 28, 3–15, 1989.
- Yahi, H., Marticorena, B., Thiria, S., Chatenet, B., Schmechtig, C., Rajot, J. L., and Crepon, M.: Statistical relationship between surface PM₁₀ concentration and aerosol optical depth over the Sahel as a function of weather type, using neural network methodology, *J. Geophys. Res.-Atmos.*, 118, 13265–13281, <https://doi.org/10.1002/2013JD019465>, 2013.
- Yang, D. and Bright, J. M.: Worldwide validation of 8 satellite-derived and reanalysis solar radiation products: A preliminary evaluation and overall metrics for hourly data over 27 years, *Sol. Energy*, 210, 3–19, <https://doi.org/10.1016/j.solener.2020.04.016>, 2020.
- Yue, X., Wang, H., Liao, H., and Fan, K.: Simulation of dust aerosol radiative feedback using the GMOD: 2. Dust-climate interactions, *J. Geophys. Res.-Atmos.*, 115, D04201, <https://doi.org/10.1029/2009JD012063>, 2010.
- Yushchenko, A., De Bono, A., Chatenoux, B., Kumar Patel, M., and Ray, N.: GIS-based assessment of photovoltaic (PV) and concentrated solar power (CSP) generation potential in West Africa, *Renew. Sust. Energ. Rev.*, 81, 2088–2103, <https://doi.org/10.1016/j.rser.2017.06.021>, 2018.
- Zhang, L., Gong, S., Padro, J., and Barrie, L.: A size-segregated particle dry deposition scheme for an atmospheric aerosol module, *Atmos. Environ.*, 35, 549–560, [https://doi.org/10.1016/S1352-2310\(00\)00326-5](https://doi.org/10.1016/S1352-2310(00)00326-5), 2001.
- Ziane, A., Necaibia, A., Sahouane, N., Dabou, R., Mostefaoui, M., Bouraiou, A., Khelifi, S., Rouabhia, A., and Blal, M.: Photovoltaic output power performance assessment and forecasting: Impact of meteorological variables, *Sol. Energy*, 220, 745–757, <https://doi.org/10.1016/j.solener.2021.04.004>, 2021.